



**Politecnico
di Torino**

Politecnico di Torino
Ingegneria Energetica e Nucleare
A.a 2020/2021
Sessione di Laurea Dicembre 2021

**Methodological development of a
digital twin for Li-ion cells
simulation: An experimental and
numerical assessment**

Relatori:
Prof. Davide Papurello
Prof. Silvia Bodoardo
Ing. Liberale Francesco De Rosa
Ing. Eduardo Graziano

Candidato:
Francesco Mazzeo

Abstract

Lithium-ion batteries are essential for the energy transition as they can be used both in the automotive field and as a stationary storage solution. They are the first choice in these sectors as they feature high energy densities, low self-discharge property, nearly zero-memory effect and long lifespan. The purpose of the thesis is to develop a procedure for the characterization of lithium-ion batteries using the GT-AutoLion tool included in the worldwide spread CAE simulation software GT SUITE. CAE simulation is a time- and cost-effective means that can support the design and testing of Li-ion cells. This methodology was defined and validated based on experimental data from coin cells assembled and tested in laboratory. In particular, charge and discharge tests at different C-RATEs and external temperatures were carried out, as well as cycle aging tests conducted exploring the impact of a different Depth of Discharge. Geometrical measurements taken on the real component and materials specifications were used to set-up a physical virtual model of the cell, calibrated and correlated against experiments. The predictivity and accuracy of this digital twin was thoroughly investigated and assessed: it was possible to model the discharge trends of the coin-cells by calibrating some fundamental parameters for cell balancing and mass transport and to estimate the degradation during constant current cycles, obtaining a very satisfactory accuracy and fitting with the experiments despite the use of non-commercial batteries ($RRMSE < 2.0\%$ and $R^2 > 0.95$). This demonstrate the potential of CAE simulation in supporting OEMs and cells manufactures in the development of their products. This work was carried out with the collaboration of the company POWERTECH Engineering S.r.l. (PWT).

Ringraziamenti

Giunto alla fine di questo cammino, ritengo importante ringraziare per primo il professore Davide Papurello, sempre disponibile, gentile e cordiale, senza il quale non avrei potuto iniziare questo percorso di tesi sperimentale. Ringrazio tutti gli ingegneri di PWT e in particolare Liberale ed Eduardo, che fin da subito mi hanno trattato come un collega e guidato nell'uso del software per la creazione del modello. Ringrazio la professoressa Bodoardo che mi ha permesso di lavorare nei laboratori del DISAT e Davide Dessantis che mi ha dato più che una mano nello svolgimento dei test sperimentali con le batterie. Ringrazio tutti i miei amici, compagni d'avventure negli anni, per esserci sempre stati e per le risate che ogni volta facciamo insieme. Ringrazio Elisabetta per avermi sempre sostenuto e sopportato alleggerendo le mie giornate nonostante il periodo difficile in cui abbiamo vissuto, restando la mia spalla in questi anni universitari ormai giunti al termine, che non scorderò mai. Infine voglio ringraziare tutta la mia famiglia per avermi concesso di vivere questa esperienza di vita prima che di studio lontano da casa, fornendomi sostegno economico ma soprattutto morale durante i momenti di difficoltà che sopraggiungono se si decide di percorrere questa via.

*Grazie di cuore, a tutti, nonostante tutto.
Francesco*

Contents

1	Introduction	8
1.1	PWT overview	8
1.2	Sustainable mobility	8
1.3	Lithium-ion batteries	11
1.3.1	LIBs Layout	15
1.3.2	LIBs glossary	18
2	Li-ion cells experimental characterization	20
2.1	Materials	20
2.1.1	Electrodes preparation	21
2.2	Coin-cell assembly	22
2.2.1	Assembly procedure	22
2.2.2	Coin-cell geometry	23
2.3	Characterization tests	25
2.3.1	Ambient temperature tests	25
2.3.2	Test at controlled temperature	27
2.4	Cycle aging tests	29
2.4.1	Aging effect on negative electrode	29
2.4.2	Aging effect on positive electrode	30
2.4.3	Cycle aging experimental tests	30
3	Li-ion Cells Modelling and Simulation in GT-AutoLion	33
3.1	GT-AutoLion	33
3.2	Lithium-ion battery model set-up	33
3.2.1	Model terminology	33
3.2.2	Theory behind the model	34
3.2.3	Overpotential	38
3.2.4	Ageing theory	38
3.3	Model Calibration and Validation on Discharge Tests	42
3.3.1	Model creation	42
3.3.2	Static calibration	45
3.3.3	Dynamic calibration	47
3.4	Model Calibration and Validation on Cycle Aging Tests	50
3.4.1	Model creation	51
3.4.2	Model results	53
3.5	GT-AutoLion Model Applications	55
3.5.1	Support to the cell design	55
3.5.2	Support to the battery management	55
3.5.3	Integration with other sub-system	57
4	Conclusion	58

List of Figures

1	Oil total final consumption by sector, 1971-2018 [3].	9
2	Transport sector CO_2 emissions by mode in the Sustainable Development Scenario, 2000-2030 [4].	9
3	Global electric vehicle stock by region (left) and Electric car share in the Sustainable Development Scenario (right) [5]. . .	10
4	Schematic representation of Li-ion cell during discharge phase with fined control volume based discretization approach. . . .	12
5	Standard conditions potentials of the most important electrodes used in batteries.	13
6	Position of the HOMO and LUMO levels of a stable and unstable electrolyte with respect to the electrochemical or Fermi potentials of the anode (left) μ_A and cathode μ_C (right). V_{OC} is the open circuit voltage.	14
7	Battery characteristic curve.	15
8	Prismatic battery.	16
9	Pouch battery.	16
10	Cylindrical battery.	17
11	Coin battery.	17
12	Example of connection of two cells in parallel and subsequently in series.	18
13	View of the jellyroll conformation of the electrodes inside the original battery.	20
14	Example of graphite electrode scraping process.	21
15	Example of a glovebox.	22
16	Coin-cell assembly.	23
17	Example of a Arbin's charge/discharge testing systems for batteries.	25
18	Discharge curves at C/5 of test 1, 3 and 4 considering all cycles.	26
19	Mean discharge curves calculated on test 1 and 3 in ambient temperature.	27
20	Example of a climatic chamber used for the controlled temperature tests.	28
21	Mean discharge curves of 45°C tests (left) and 5°C test (right).	29
22	Cycle aging methodology.	31
23	Capacity degradation in cycle aging tests.	32
24	Cross-Sectional representation of Pseudo-2D model of a Lithium-ion cell.	35
25	SEI growth and Li plating degradation phenomena.	41
26	Calibration model on GT-AutoLion.	43
27	Compilation of active material templates in GT-AutoLion modeling software.	43

28	C/20 simulation discharge curves at ambient temperature (left) and 45°C (right) versus all experimental curves considered for the calculation of the mean one.	47
29	C/10 and C/5 simulation discharge curves at ambient temperature (left) and 45°C (right) versus all experimental curves considered for the calculation of the mean one.	49
30	Calibration model for degradation phenomena.	52
31	Example of configuration of the anodic template with degradation phenomena.	52
32	Results of the calibration of cycle aging between SOC 100-0 (left) and 90-10 (right).	55
33	Sensitivity of the calibrated model at ambient temperature and 45°C (C/5 curves) to the variation in the diameter of the particles that make up the NMC622 (left) and graphite (right)	56
34	Simulated SOH at various DOD.	57
35	Model of a BEV created in GT-AutoLion.	58

List of Tables

1	Initial geometric dimensions.	24
2	Geometric dimensions of the second test.	24
3	Test structure at ambient temperature.	26
4	Test structure at 45°C and 5°C.	28
5	Structure of cycle aging tests.	31
6	Starting, boundaries and design value for the static calibration parameters.	46
7	Statistical parameters to evaluate the results of the static calibration.	47
8	Starting, boundaries and design value for the dynamic calibration parameters.	48
9	Statistical parameters to evaluate the results of the dynamic calibration.	50
10	Starting, boundaries and design value for the cycle aging calibration parameters.	54
11	Statistical parameters to evaluate the results of the cycle aging calibration.	54

1 Introduction

1.1 PWT overview

Founded in 2007 as a spin-off of Politecnico di Torino, PWT is nowadays an independent consulting firm providing services in the field of powertrain and vehicle simulation. PWT works in tight collaboration with automotive OEMs and their R&D teams, at different stages in the development of new products and technologies and gives its support on and off-site projects, develops new simulation methodologies or directly shares those that have been established in PWT's multi-year experience. PWT is today an expanding and dynamic company with an international reach, being present with its services in more than 10 countries and three continents around the world. Nowadays the CAE simulation is a key factor in the virtualization of the product development process, reducing R&D costs and shortening time-to-market of innovative technologies. In this perspective, the development of reliable simulation tools for electrified, electric or hydrogen-powered vehicles is PWT's main focus and objective [1].

1.2 Sustainable mobility

The concept of sustainable mobility has much older origins than what is thought, already in 1992 the EU commission in a green paper launched the concept of *"sustainable mobility"* and in particular highlighted the need: *"to reduce the harmful effects of the transport sector on the environment by promoting fast, safe and convenient urban and regional transport services and reducing urban car traffic"* [2]. Unfortunately, from 1990 to today, according to the data of the International Energy Agency (IEA) the impact of the transport sector on the oil total final consumption (TFC) has increased [3]. An increase in the TFC of oil implies, despite the production of increasingly efficient transport systems, a growth in the production of CO_2 , of which the transport system is responsible for 24% of direct emissions from fuel combustion. The IEA itself has created a sustainable scenario that develops until 2030 capable of perfectly respecting the Paris agreements by keeping the global average temperature rise below $2^\circ C$. This scenario also provides for a reduction in emissions from the transport sector shown in figure 2 [4]. As can be seen, among transport, the greatest contribution is due to passenger road vehicles, to achieve a reduction in emissions it is necessary to increase the quantity of vehicles powered by alternative fuels such as hydrogen or bioethanol and, of course, batteries. The latter in particular has been growing rapidly over the past ten years, with 10 million on the world's roads at the end of 2020. Electric car registrations increased by 41% in 2020, despite the pandemic-related worldwide downturn in car sales in which global car sales dropped 16%. Around 3 million electric cars were sold globally (a 4.6% sales share), and Europe overtook the People's Republic of China

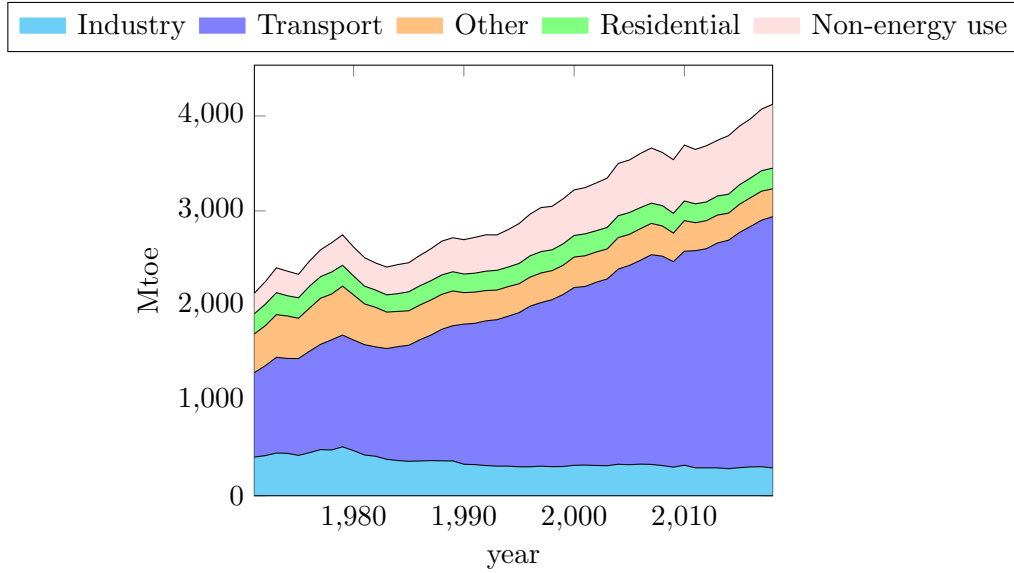


Figure 1: Oil total final consumption by sector, 1971-2018 [3].

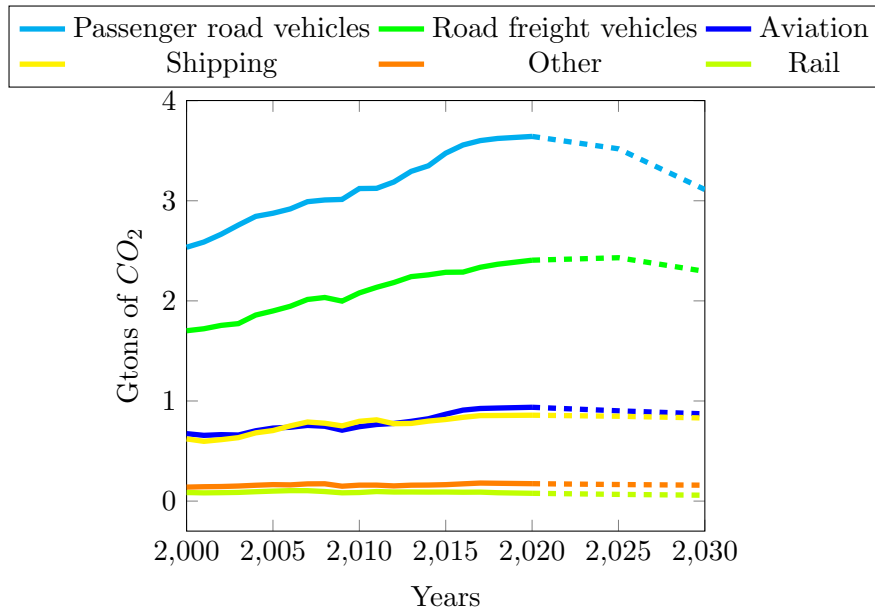


Figure 2: Transport sector CO_2 emissions by mode in the Sustainable Development Scenario, 2000-2030 [4].

as the world's largest electric vehicle market for the first time (figure 3). Obviously these numbers are destined to increase and according to the IEA sustainability scenario in 2030 they will exceed 10% of the total share of transport vehicles [5].

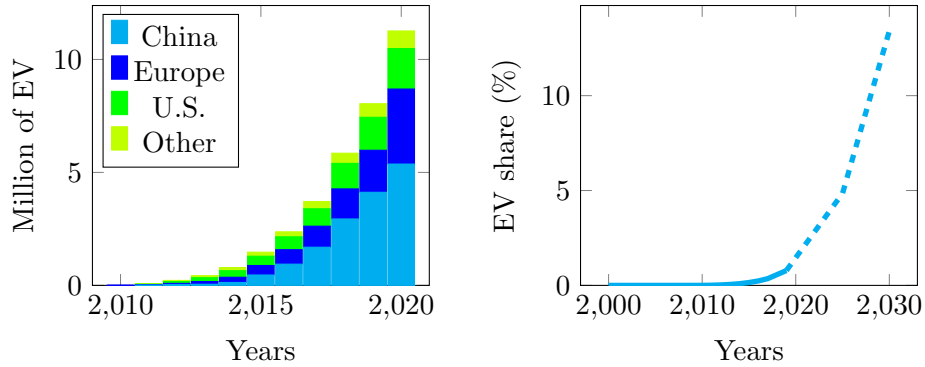


Figure 3: Global electric vehicle stock by region (left) and Electric car share in the Sustainable Development Scenario (right) [5].

Having understood how important electric vehicles will be for the energy transition, it is also important to investigate the types of electric vehicles currently on the market. In particular they are distinguished in:

- **Battery electrical vehicle (BEV):** it's a vehicle that is entirely powered by a battery pack and has an electric motor as its propeller. Its autonomy is limited by the battery capacity and not being equipped with an internal combustion engine (ICE), it has no direct emission during its use.
- **Plug-in Hybrid Electric Vehicle (PHEV):** it's a vehicle that features a hybrid propulsion consisting of a battery-powered electric motor and an ICE. The vehicle can exploit only the electric propulsion, the ICE or both for this reason the battery pack can be recharged externally and has a discrete capacity but not as large as the BEV. The emissions during its use are reduced but not zero if the internal combustion engine is working.
- **Full Hybrid Electric Vehicle (FHEV):** it's a vehicle that has a hybrid electric and thermal propulsion and it's possible to travel using only the electric motor for very short distances. The battery has a low capacity compared to PHEV and can only be recharged while the vehicle is being used by the ICE and regenerative braking. Direct emissions are contained but are never zero.
- **Mild Hybrid Electric Vehicle (MHEV):** it's a vehicle that has a hybrid electric and thermal propulsion but it is not possible to travel

using only the electric powertrain even for short distances. The electric motor has the sole purpose of supporting the ICE and the batteries are recharged by the latter or in regenerative braking.

All these types of vehicles have in common the presence of an electric motor power battery, which is essential for the operation of hybrid vehicles such as full electric ones. Among the main types of batteries, the most common in the automotive sector are certainly lithium-ion batteries.

1.3 Lithium-ion batteries

Lithium-ion batteries (LIBs) are a type of rechargeable battery that exploits redox reactions for the transformation of the chemical energy of the reactants into electrical energy, essentially a galvanic cell. The processes that take place in a galvanic cell are spontaneous, as they do not need an external electric current to be imparted to the cell to take place, so the Gibbs free energy difference associated with these processes is less than zero [6]. LIBs, as illustrated in figure 4 are composed of three main compartments:

- A porous positive electrode called cathode in which the reduction half-reaction takes place during the discharge phase.
- A porous negative electrode called anode in which the oxidation half-reaction takes place during the discharge phase.
- A separator, usually in polyethylene and polypropylene, that allows the passage of only lithium ions and avoids direct contact between the electrodes.

The cell is commonly filled with an electrolyte made of solvent and Li-salt to facilitate the mobility of Li-ions allowing the diffusion towards the separator.

As shown in figure 4, the active materials are deposited on the current collectors, which do not actively participate in the electrochemical reactions but which are essential for the passage of current and for the consistency of the electrode itself. Usually the materials of the collectors are copper for the anode and aluminum for the cathode. The active materials can be various and are important as they determine the reactions that take place at the anodic and cathodic interface which are characterized by a variation of gibbs free energy which determines the potential of the reaction that in standard conditions ($T = 25^{\circ}C$, $p = 1atm$) can be calculated with the Nernst equation:

$$E^0 = -\frac{\Delta G^0}{zF} \quad (1)$$

Where z is the number of electrons exchanged in the reaction, F is Faraday's constant (96487 Coulomb) and E_0 is the voltage generated by the reaction.

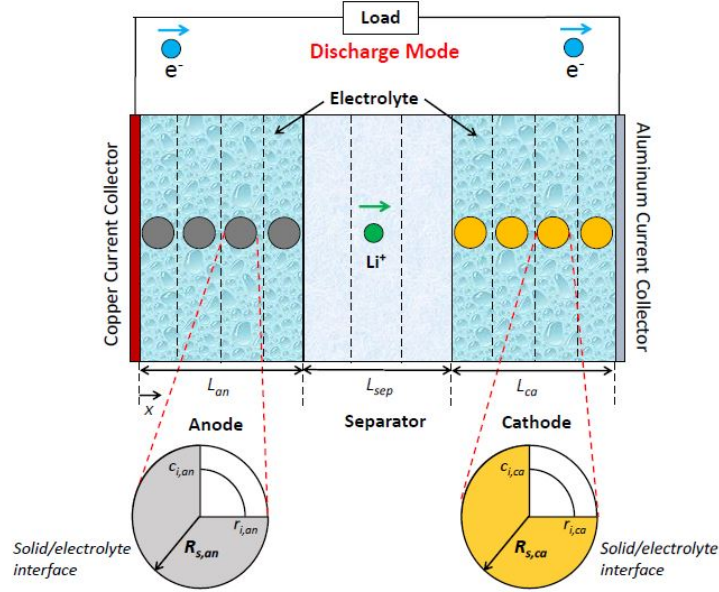


Figure 4: Schematic representation of Li-ion cell during discharge phase with finned control volume based discretization approach.

Under different thermodynamic conditions, the Nernst equation becomes:

$$E = E^0 - \frac{RT}{zF} \ln\left(\frac{\prod_{n=1}^P a_i^{\nu_i}}{\prod_{n=1}^R a_i^{\nu_i}}\right) \quad (2)$$

Where at the logarithm argument there is the product of the activity of the species (a_i) produced at the numerator and of the reactant species at the denominator elevated the stoichiometric coefficients of the reaction (ν_i). Therefore the voltage generated in a cell depends on the reactants and the products, taken as a reference of potential 0 the reaction: H_2/H^+ in aqueous solution, the reaction potentials of various materials that can be used as electrodes in lithium ion batteries can be defined and are shown in the figure 5. It highlights the reactions with the respective potentials of the active materials most used in lithium-ion batteries. Generally the cathode is made of metal oxides which at first were entirely based on cobalt ($LiCoO_2$), subsequently due to the cost of production of the latter it was decided to reduce it by mixing with nickel and manganese (NMC) and with nickel and aluminum (NCA), mainly used in the automotive sector. Instead the anode consists mainly of carbon in the form of graphite [7]. An important issue when considering the materials to be used for the battery is the chemical stability of the cell that is achieved only when the chemical potentials of the anode and cathode fall within the energy range (or gap) of the electrolyte, in order to prevent it from having unwanted reactions. Knowing that a chemical bond is established when a HOMO orbital (highest occupied molecular

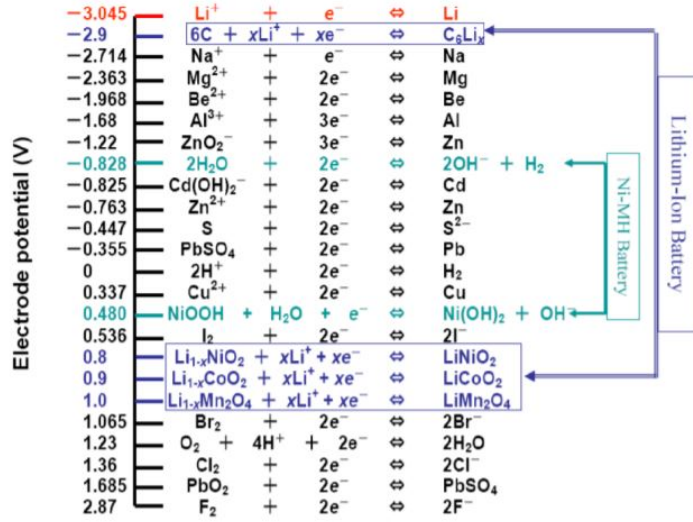
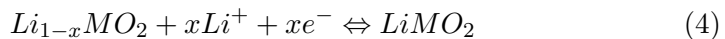
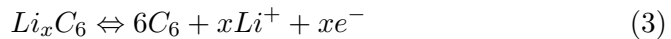


Figure 5: Standard conditions potentials of the most important electrodes used in batteries.

orbital) of one molecule interacts with the LUMO orbital (lowest unoccupied molecular orbital) of another reacting molecule, if the electrolyte had the lowest unoccupied level (LUMO) below the reaction potential of the anode μ_A (Fermi level of the anode) the reduction would occur and the electrons would be released from the electrolyte itself; in the same way there would be oxidation by the cathode which would tear electrons from the electrolyte if μ_C is lower than the highest occupied level (HOMO).

A large gap between the LUMO and the HOMO of a liquid electrolyte (or similarly between the conduction band and valence for a solid electrolyte), allows to use anodes and cathodes with high differences between Fermi levels, thus increasing the potential difference of the cell.

The operation of lithium-ion batteries is very simple and is the same as that of any electrochemical cell. During the charging process, the lithium ions move from the cathode, through the electrolyte, to the anode, and then return during discharge. The process of accepting the lithium ions by the two materials that make up the electrodes is called *intercalation*. The discharge/charge half reactions for a graphite anode and a cathode composed of an oxide of a generic metal M are the following:



The equations 3 and 4 represent the discharging process from left to right, while the charging process on the contrary. To make such reactions take place, an external circuit connected to a load (for example a resistance) is

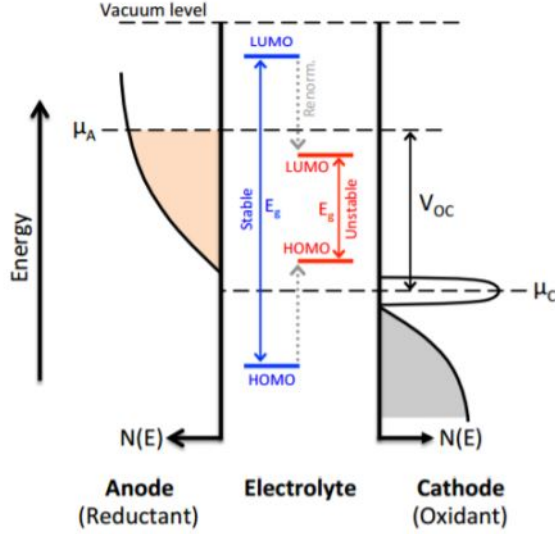


Figure 6: Position of the HOMO and LUMO levels of a stable and unstable electrolyte with respect to the electrochemical or Fermi potentials of the anode (left) μ_A and cathode μ_C (right). V_{OC} is the open circuit voltage.

needed that conveys the electrons from one collector to the other, while a generator is needed in the charging phase to provide the energy necessary to reverse the reactions being that the free energy of Gibbs associated with this phenomenon is greater than zero and therefore the reaction is not spontaneous. The open circuit voltage (OCV) generated by the reactions, as already mentioned, can be calculated from the equation 2. In reality, the battery does not always have this potential which refers only to the equilibrium conditions of the cell (i.e. when it doesn't operate) but it is noted that the latter is a function of the state of charge, the current and the temperature [?]. During its operations, losses occur which are called overpotentials that lead to voltage drops with respect to the ideal one in OCV, the characteristic curve of a battery is therefore defined as *polarization curve* whose trend is shown in figure 7. Then the actual battery voltage can be rewritten as

$$V = OCV - V_{act} - V_{ohm} - V_{conc} \quad (5)$$

Where

- V_{act} : It's the activation overpotential that is needed to start the reaction and is the cause of the initial exponential drop.
- V_{ohm} : It's the ohmic overpotential due to the diffusion of ions through the battery, it is therefore a resistive loss and is the cause of the linear voltage drop.

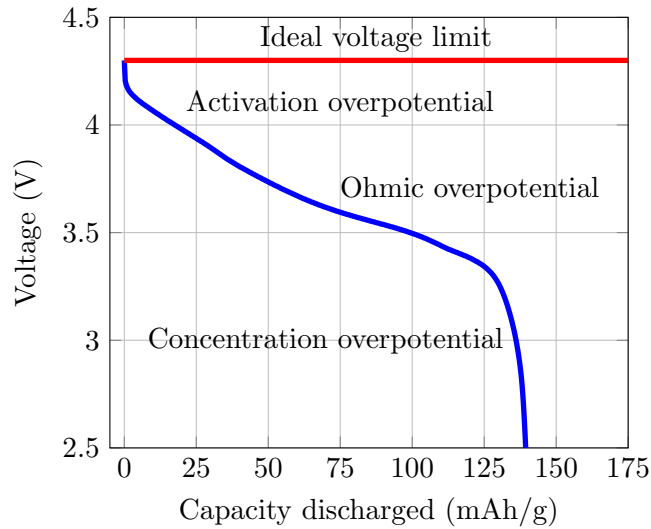


Figure 7: Battery characteristic curve.

- V_{conc} : It's the concentration overpotential, it appears when the battery is close to its nominal capacity and is due to the low concentration of ions near the electrode (now almost all migrated to the cathode) which take longer to react leading to another exponential voltage drop.

These losses will be analyzed in detail and modeled in the chapter 3.

1.3.1 LIBs Layout

Lithium batteries are internally made up of several stacks where the cathode, anode and separator are enclosed in a laminated film. The case of the LIBs can have different shapes depending on the use: prismatic, pouch, cylindrical or coin.

- **Prismatic:** Prismatic container usually made of aluminum or thin steel for excellent internal heat dissipation. Available in any size, from the smallest such as those found in mobile phones, up to very large sizes. Capacities ranging from 0.8 Ah up to even values of 100 Ah. Their shape allows them to optimize space and allows flexibility in the design of the battery pack.
- **Pouch:** Very thin cells, without rigid parts that allow to have a very low weight. Given their structure are replacing the prismatic ones in the application in electric vehicles. Their high surface is able to dissipate heat quickly, but from a mechanical point of view they are disadvantaged given their fragility, therefore the battery pack must be built paying attention to protection from possible impacts

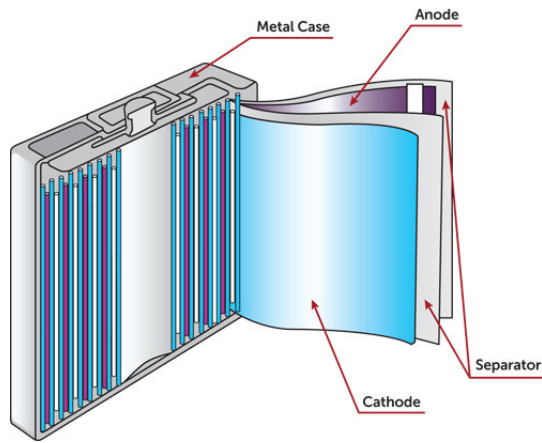


Figure 8: Prismatic battery.

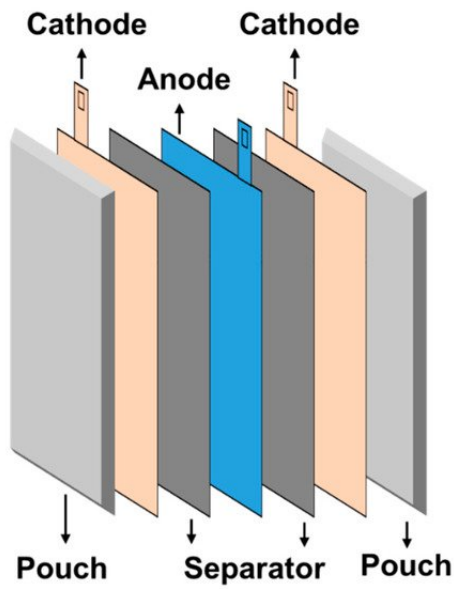


Figure 9: Pouch battery.

- Cylindrical:** Cylindrical are the most commonly used batteries, especially given their low production cost although they have lower average energy densities than previous types. Their shape allows good thermal stability and resistance to internal pressure stresses without deforming. These batteries are used in various fields of application: medical instruments, laptops and of course in the automotive sector, in fact all Tesla cars are equipped with them [REF].

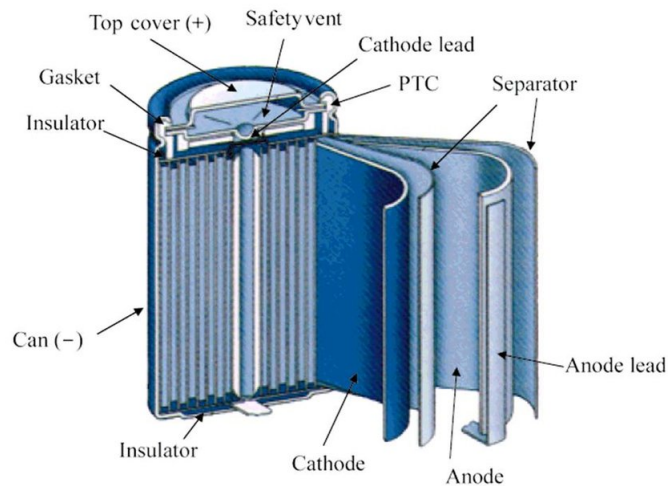


Figure 10: Cylindrical battery.

- Coin:** A coin battery is a small single cell battery shaped as a squat cylinder typically 5 to 25 mm (0.197 to 0.984 in) in diameter and 1 to 6 mm (0.039 to 0.236 in) high—resembling a coin. Stainless steel usually forms the bottom body and positive terminal of the cell, and an insulated top cap is the negative terminal. Are used to power small portable electronics devices such as wrist watches and pocket calculators.

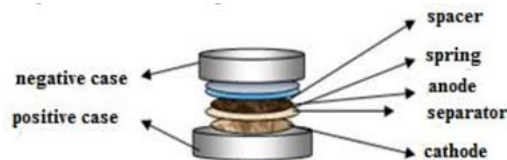


Figure 11: Coin battery.

Each battery is capable of generating a voltage that is limited by the theoretical one of the reaction of the materials that make up the electrodes

(figure 5) and a capacity that is limited by the weight of the active materials and their area. For this reason, to increase the voltage for applications that require more power, it is necessary to connect several batteries in series while to increase their capacity it is necessary to connect several batteries in parallel.



Figure 12: Example of connection of two cells in parallel and subsequently in series.

1.3.2 LIBs glossary

The LIBs, in addition to being categorized by the materials that make up the cathode and the electrolyte, are characterized by fundamental parameters that must always be taken into consideration when it's desired to carry out an analysis on the battery.

- **Battery pack:** Electric vehicles and HEVs have a high voltage battery pack consisting of individual modules and cells organized in series and in parallel. A module consists of multiple cells linked in series or parallel. A battery pack is then assembled by re-connecting the modules in series or in parallel.
- **Secondary and Primary Cells:** Although it may not sound like it, batteries for hybrid, plug-in, and electric vehicles are all secondary batteries. A primary battery is one that can not be recharged. A secondary battery is one that is rechargeable.
- **C-RATE:** In describing batteries, discharge current is often expressed as a C-rate in order to normalize against battery capacity, which is often very different between batteries. A C-rate is a measure of the rate at which a battery is discharged relative to its maximum capacity. A 1C rate means that the discharge current will discharge the entire battery in 1 hour. For a battery with a capacity of 100 Ah, this equates

to a discharge current of 100 A. A 5C rate for this battery would be 500 A, and a C/2 rate would be 50 A. It has the units h^{-1} .

- **State of Charge (SOC)(%)**: An expression of the present battery capacity as a percentage of maximum capacity. SOC is generally calculated using current integration to determine the change in battery capacity over time.

$$SOC = \frac{\int_0^t i(t)dt}{C_{max}} \quad (6)$$

- **Depth of Discharge (DOD) (%)**: The percentage of battery capacity that has been discharged expressed as a percentage of maximum capacity. A discharge to at least 80% DOD is referred to as a deep discharge.
- **State of health (SOH) (%)**: State of health (SOH) is a figure of merit of the condition of a battery (or a cell, or a battery pack), compared to its ideal conditions. The units of SOH are percent points and so a SOH=100% means that the battery's conditions match the battery's specifications). Typically, a battery's SOH will be 100% at the time of manufacture and will decrease over time and use.
- **Terminal voltage (V)**: The voltage between the battery terminals with load applied. Terminal voltage varies with SOC and discharge/charge current.
- **Open Circuit Voltage (OCV) (V)**:The voltage between the battery terminals with no load applied. The open-circuit voltage depends on the battery state of charge, increasing with state of charge.
- **Internal resistance**: The resistance within the battery, generally different for charging and discharging, also dependent on the battery state of charge. As internal resistance increases, the battery efficiency decreases and thermal stability is reduced as more of the charging energy is converted into heat. It is due to the effects of various overpotentials.

2 Li-ion cells experimental characterization

2.1 Materials

The batteries under study are coin-cells composed of the following materials:

- Cathode: Nickel manganese cobalt with a mass percentage respectively 60%, 20%, 20%, hereinafter referred to as NMC622.
- Anode: Graphite.
- Separator: Celgard 2325, a polymeric membrane used to allow the passage of lithium ions.
- Electrolyte: Aqueous Lithium hexafluorophosphate $LiPF_6$ in ethylene carbonate (EC)–ethyl methyl carbonate (EMC) 1M concentration.

The materials belonged to the battery of a Fiat 500 BEV, with an undefined mileage. They were removed from the original battery case and treated to remove the liquid electrolyte they were soaked in. The electrodes are in the form of thin sheets with a thickness of a few hundred micrometers folded on themselves to form the so-called "Jellyroll".

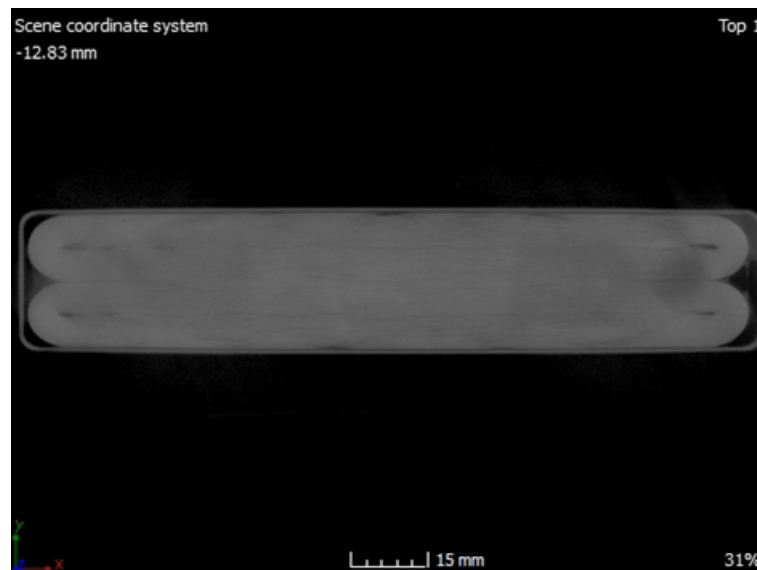


Figure 13: View of the jellyroll conformation of the electrodes inside the original battery.

Each electrode is composed of two external layers of active material spread over their respective collectors: copper for graphite and aluminum for NMC622. It's clear that to obtain electrodes for a coin-cell, a layer of

active material must inevitably be removed. In the following sub-chapters the methodologies for the final treatment of the original electrodes will be analyzed to make them compatible with the geometry of a coin-cell.

2.1.1 Electrodes preparation

The process for the production of the coin-cell's electrodes can be summarized as follows.

1. **Scraping:** The electrode sheet is cut and the most deteriorated part is placed upwards on a steel plate and fixed to the edges. The surface layer of graphite is then scraped by hand, using a spatula, until the copper sheet is visible while the surface layer of NMC622 is wetted with liquid solvent that does not affect its properties (N-methyl pyrrolidinone, NMP) and then scratched off with sandpaper. The processes are started from the edges where the electrodes are mostly damaged and is completed when only one layer of collector remains with the other one of active material underneath.



(a) Anode electrode before treatment. (b) Anode electrode after treatment.

Figure 14: Example of graphite electrode scraping process.

2. **Cut:** The electrode sheets, now composed of a layer of copper/aluminum and one of graphite/NMC622, is inserted into a die-cutting machine in order to obtain discs with a predetermined diameter.
3. **Drying:** The electrode disks are placed in a dryer where they remain in vacuum conditions at 120°C for 4 hours. This is because the assembly of the coin cell takes place inside a glovebox in which there is a controlled environment devoid of oxygen and water.

2.2 Coin-cell assembly

Assembling the coin-cell is the most delicate part of creating the battery. Being a manually process, particular attention must be paid to aligning all the elements that make up the geometry of the cell to obtain maximum performance. As already mentioned, the assembly takes place inside the "glovebox", a sealed container, specially designed and built to handle instruments and substances in a confined environment completely separate from that in which the operator is located.



Figure 15: Example of a glovebox.

The glovebox is necessary to avoid the interaction of electrolytes that contain lithium with oxygen and nitrogen present in the atmosphere, giving rise to reactions that can cause deterioration of performance or more dangerous one such as fires [9]. Once the battery is created, the case is placed in an automatic press where it will be closed with a pressure of 5.5 bar.

2.2.1 Assembly procedure

Although tests have been made to verify the best geometry to testing the coin-cells, the internal conformation remains standard and the assembly process can be divided into various steps.

1. The part of the case that will be negative is placed on the work surface.

2. A steel gasket and a steel spacer are placed inside the case.
3. The negative electrode is inserted with the copper part in contact with the spacer.
4. $10 \mu L$ of electrolyte is poured onto the graphite through a pipette.
5. The separator composed of a polymeric membrane, which has the task of allowing the passage of the lithium ions from one electrode to the other through the electrolyte, is placed above the graphite-copper disk.
6. $40 \mu L$ of electrolyte is poured onto the separator through a pipette.
7. The positive electrode is inserted with the active material part in contact with the separator.
8. Another spacer is placed over the positive electrode in contact with the Aluminium part.
9. Everything is closed with the other part of the case which will be the positive one.

To have a clearer view, the various parts of the coin-cell are schematized in the figure below.

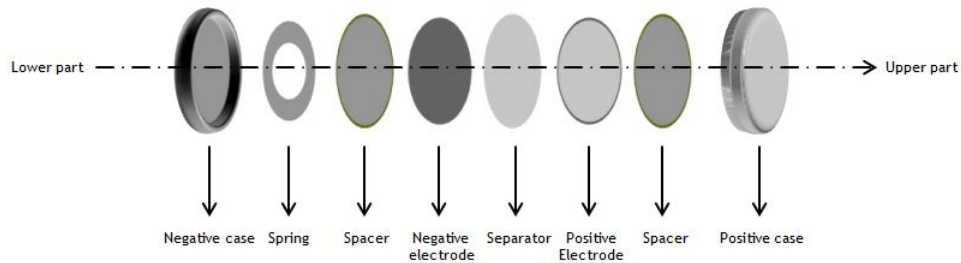


Figure 16: Coin-cell assembly.

The one shown in the figure 16 is the composition of the coin-cells created for the purpose of the case study and will be defined as *standard* from now on.

2.2.2 Coin-cell geometry

So far we have analyzed the process of creating the coin-cell, but it is also necessary to analyze the geometric part (i.e. the dimensions) of the battery

Table 1: Initial geometric dimensions.

Components	Diameter [mm]	Thickness [μm]
First spacer	15.5	500
Negative electrode	18	87
Separator	20	20
Positive electrode	15	77
Second spacer	15.5	500

components. Various geometries were tested to identify the best one to use in subsequent tests.

The coin cells created with the standard assembly and the layout shown in the table 1 showed bad results: No cell was able to reach the state of charge corresponding to a voltage equal to 4.3V and many after being pressed went into short circuit. Disassembling some cells, it has been noticed that the graphite disk, having a diameter approximately equal to that of the case and of the separator, was damaged during closing or goes into direct contact with the NMC622 causing short circuits. This is because the assembly procedure is manual, making it very easy to misalign the various components. Since the problem is the diameter of the negative electrode, it was decided to reduce it, due to instrumental constraints the second geometry tested foresees a diameter for the graphite and copper disk equal to 15mm, exactly equal to that of NMC622 and aluminum.

Table 2: Geometric dimensions of the second test.

Components	Diameter [mm]	Thickness [μm]
First spacer	15.5	500
Negative electrode	15	87
Separator	20	20
Positive electrode	15	77
Second spacer	15.5	500

With this geometry it was possible to carry out characterization tests up to currents of 1C, at which the results began to become poor. To try to solve this problem, it was decided to act on the assembly, inserting another spacer with a thickness of 0.2 mm in the side of the cathode electrode to achieve greater adhesion between the various layers. However, the results were disappointing and it has been decided to return to the standard assembly, with the geometry shown in table 2, which will also be referred as *standard* from now on. An important clarification concerns the thickness of the various materials, as regards the electrodes the values shown in tables 1 and 2 are the result of previous studies while as regards the spacers and the separator

the values have been taken from the respective datasheets [Possible cite].

2.3 Characterization tests

In order to create a model of the batteries using the software GT-AutoLion it is first necessary to collect experimental data, in particular characteristic curves (Voltage-Capacity, figure 7) curves are needed, obtained at various C-RATEs and temperatures. Using standard assembly and geometry, coin-cells were created through the process described in chapter 2.2.1 and inserted into an ultra-high precision charge/discharge testing systems from Arbin instrument [11] that is capable of give a constant charging and discharging current corresponding to the desired C-RATEs between 2.5V and 4.3V that are assumed to be the voltages corresponding to SOC=0% and SOC=100%.



Figure 17: Example of a Arbin's charge/discharge testing systems for batteries.

Since the battery capacity is unknown before testing it, to calculate the currents corresponding to the desired C-RATEs, it was decided to use the electrode with the lowest ideal specific capacity as a reference, i.e. the NMC622 with 175 mAh/g compared to the 350 mAh/g of graphite, since the electrodes are of the same size, it is certainly the one that limits the battery capacity. During the creation of the coin-cell, the NMC622 disk was weighted (excluding the aluminum collector) and the battery capacity was calculated, from the latter the currents expressed in C-RATE were obtained and used in the Arbin ciclator.

2.3.1 Ambient temperature tests

As already mentioned, the temperature also has an important influence on the charaterization curves. Unfortunately, the use of the climatic chamber is limited and it was preferred to use it for temperatures such as 45°C and 5°C. Therefore, the first characterization tests were carried out at room temperature and due to technical limitations it was not possible to monitor

it. The currents chosen for all the characterization tests were C/20, C/10, C/5, C/2 and 1C, where for each C-RATE several charge and discharge cycles were carried out and can be summarized in table 3.

Table 3: Test structure at ambient temperature.

(a) Structure of the first to the third test.			(b) Structure of the fourth test.		
C-RATE	Cycle	Time [h]	C-RATE	Cycle	Time [h]
C/20	3	120	C/20	5	200
C/10	3	60	C/10	4	80
C/5	3	30	C/5	4	40
C/2	3	12	C/2	4	16
1C	3	6	1C	4	8

The battery of the second test exhibited a deterioration in capacity which led to the conclusion with no analyzable results. In the fourth test more cycles were carried out at the various C-RATES to have more data on which to calculate the average discharge curves, as it must be considered that the first cycles at C/20 are for the formation of the battery as it is new and could not reflect the true capacity of the latter. Furthermore, another goal is to evaluate the behavior at higher C-RATES as the number of formation cycles at low C-RATE increases.

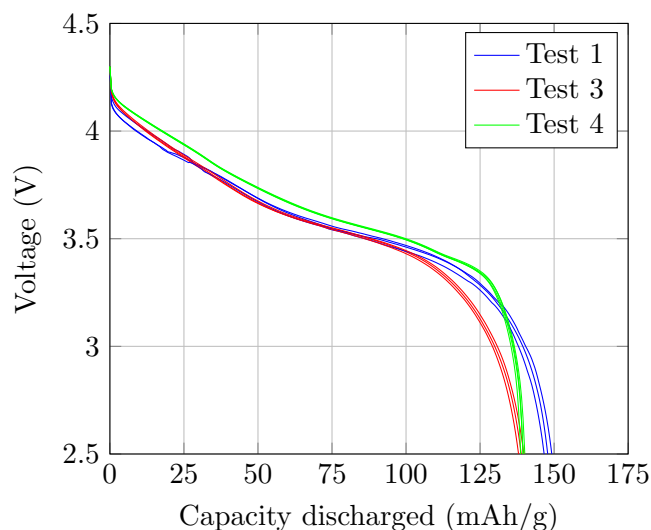


Figure 18: Discharge curves at C/5 of test 1, 3 and 4 considering all cycles.

As can be seen from figure 18, the battery of test 4 in comparison with the other batteries has a lower internal resistance which results in a lower slope of the central part and a worse diffusivity, which results in the more

pronounced drop in tension in the final part of the curve. In any case, despite the sudden drop, it has reached higher specific capacity at $C/2$ and $1C$. For these completely different trends, it was decided to exclude the results of this test from the calculation of the total mean curves for each C-RATE taking into consideration only test 1 and 3. The discharge curves are presented in figure 19.

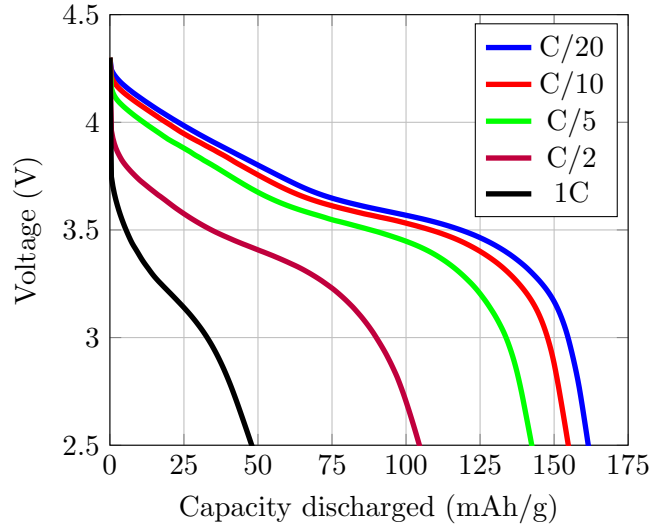


Figure 19: Mean discharge curves calculated on test 1 and 3 in ambient temperature.

It's immediately clear how the curves at $C/2$ and $1C$ show a decrease in specific capacity greater than the others. This effect is very marked and is probably due to the deterioration of the materials that have been cycled an indefinite number of times and the manual creation process that clearly leads to worse performance than one might expect from commercial batteries [10].

2.3.2 Test at controlled temperature

As already anticipated, other characterization tests were carried out at a controlled temperature of 45°C and 5°C in a climatic chamber.

The temperature has an important effect on the performance of the batteries, especially at higher currents, as it improves the diffusive phenomena and therefore the transfer of charge and ions through the separator, the electrolyte and the electrodes [10]. Two tests were carried out at 45°C because due to an error in the cycler setting, during the first test the currents corresponding to $C/2$ and $1C$ are saturated to a value equal to $C/2.3$ while only one test was carried out at a temperature of 5°C .

As can be seen from the table 4a, for the first test at 45°C fewer cycles were performed at the lowest C-RATES to reduce the time of the experiment



Figure 20: Example of a climatic chamber used for the controlled temperature tests.

Table 4: Test structure at 45°C and 5°C.

(a) Structure of the first test at 45°C.

C-RATE	Cycle	Time [h]
C/20	2	80
C/10	2	40
C/5	2	20
C/2	3	12
1C	3	6

(b) Structure of the other tests

C-RATE	Cycle	Time [h]
C/20	3	120
C/10	3	60
C/5	3	30
C/2	3	12
1C	3	6

for logistical reasons for the use of the climatic chamber. In any case, the two tests showed similar results, differing slightly in the various C-RATES and cycles. The mean curves of all tests at 45°C and those of the test conducted at 5°C are shown in figure 21.

From the figure 21 on the right, it becomes clear that the results of the test conducted at 5°C are extremely bad. The specific capacity at C/20 is less than 100 mAh/g, very similar to the value of the curve at 1C at 45°C on the left. Clearly the effect of the lower temperature should lead to worse performances but they do not justify those obtained by the coin-cell [10], so they will not be considered in the subsequent calibration of the model discussed in chapter 3. Another important aspect to underline is that the curves at C/2 and 1C of the test at 45°C once again show a substantial decrease in capacity compared to the other C-RATES. The reasons are the same as explained in the chapter 2.3.1 and so these data-sets will also be excluded in the model calibration process, taking into consideration only the discharge curves up to C/5.

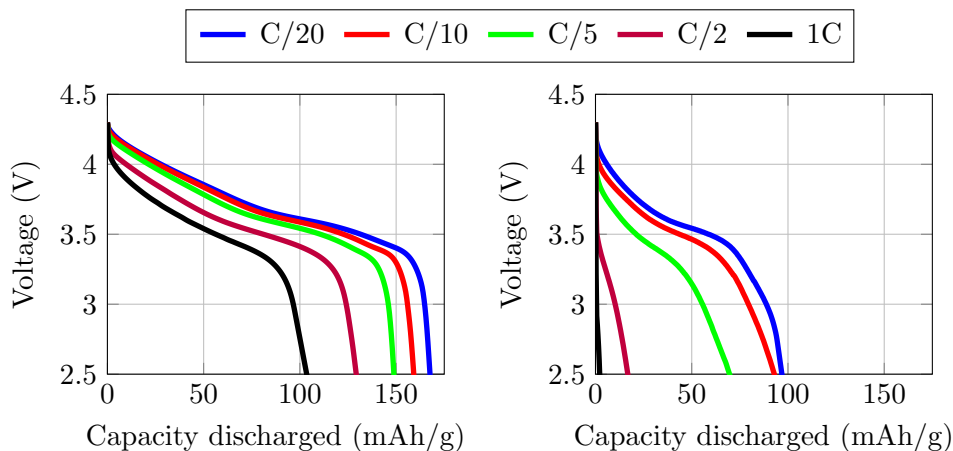


Figure 21: Mean discharge curves of 45°C tests (left) and 5°C test (right).

2.4 Cycle aging tests

The cycle aging tests are special tests where it's desired to evaluate the life of the battery when it is subjected to various charge and discharge cycles. During its use, the battery is subjected to degradation phenomena that can be both mechanical and chemical, leading to a reduction in useful capacity. One of the main effects of battery aging is the degradation of the electrode, which can therefore lose active material that dissolves in the electrolyte, such as for example manganese. In any case the degradation mechanisms are many and they are different between positive and negative electrode and are strongly favored by high temperatures and states of charge (SOC > 80%) [12].

2.4.1 Aging effect on negative electrode

The negative electrode, which in this study is graphite, is the main subject of the degradation phenomena, which are:

- The growth over time at the electrolyte/electrode interface of a solid layer called "Solid Electrolyte interface" (SEI). This interface is created naturally during the first charge and is useful for increasing the safety of the battery as it is a natural barrier between the electrolyte and the electrode [13]. During operations, the electrode particles suffer from volume changes that induces mechanical stresses, that causes the SEI to break and the exposure of fresh graphite surface to the electrolyte that cause a formation of new SEI and the consumption of ions. In any case, SEI is permeable to lithium ions, which however, with the growth of the latter, have to travel further to reach graphite, worsening its diffusivity. Therefore, the growth of the SEI layer induces losses of

lithium ions, decomposition of the electrolyte and worsening of diffusive phenomena [14]. In any case, the growth is relatively stable over time if the battery operates in the voltage ranges that correspond to the electrochemical stability of the electrolyte [15], therefore the loss of capacity because of the SEI growth is not significant in short terms.

- Loss of active material over time. This phenomenon concerns the decomposition of material that is no longer available for the insertion of lithium due to the breakage of the particles, the loss of electrical contact or the obstruction of the active sites from other resistive layers and involves an increase in the impedance of the electrode and can occur during cycles as during battery storage periods [16]. It is favored at high states of charge (SOC>80%) due to the high potential difference between electrode and electrolyte [17].
- Lithium plating, that is the formation of metallic lithium around the anode which can be homogeneous or heterogeneous. During the charging process, lithium ions from the cathode are inserted into compounds with layered structures in the anode. During this process, which is called intercalation, is when lithium plating takes place. The phenomena is favored at high charge current due to the forcing of lithium ions to move at a faster reaction rate and accumulate in the surface of the anode and during charging at low temperature, that slows down the reaction rate affecting the intercalation of lithium ions [18].

2.4.2 Aging effect on positive electrode

The degradation phenomena are less influential on the positive electrode and are approximately the same as those occurring at the anode, i.e. the creation of the SEI layer, loss of active material and the consequent degradation of the electrolyte. These effects are not independent of each other and strongly depend on the type of active material used [19].

2.4.3 Cycle aging experimental tests

To estimate the effect of these phenomena, it was decided to use the cycle aging test. The execution method provides for charge and discharge cycles in constant current (CC) carried out respectively at C-RATE of C/10 and C/5 and it's schematized in figure 22.

Therefore from this test it is possible to obtain a trend of the degradation of the capacity cycle after cycle. It's important to specify that this methodology is a readjustment, due to both time and battery requirements, of a more precise methodology developed by ENEA to which reference should be made for completeness [20]. From commercial batteries subjected to such

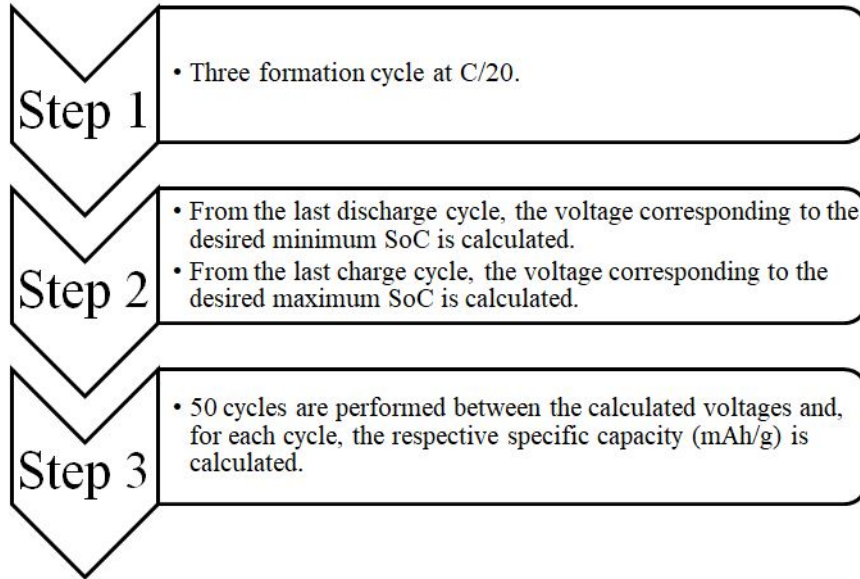


Figure 22: Cycle aging methodology.

tests, a deterioration of 20% from nominal capacity is expected after approximately 1000 cycles performed at currents higher than 1C [21]. Dealing with experimental batteries composed of materials already cycled and assembled manually, an exponential deterioration is obtained which leads to a loss of capacity greater than 40% after 50 cycles, probably due to the loss of anode and cathode active material, so it was possible to obtain results in a short time. As already mentioned, the degradation phenomena are influenced by the temperature and the state of charge. Since it was not possible to act on the first which is therefore that of the surrounding environment, it was instead acted on the state of charge, cycling the batteries between different SOC.

Table 5: Structure of cycle aging tests.

Assembly	Geometry	SOC (%)	Voltages (V)	cycles
Standard	Standard	100-0	4.30-2.50	50
Standard	Standard	90-10	4.19-3.32	50
Standard	Standard	80-20	4.04-3.42	50

The table 5 summarizes the details of the individual cycle aging tests carried out. The battery health (SOH) results are shown in the figure below.

From the trends of the degradation curves shown in the figure 23, the effect of the depth of discharge (DOD) can be immediately noted. Higher

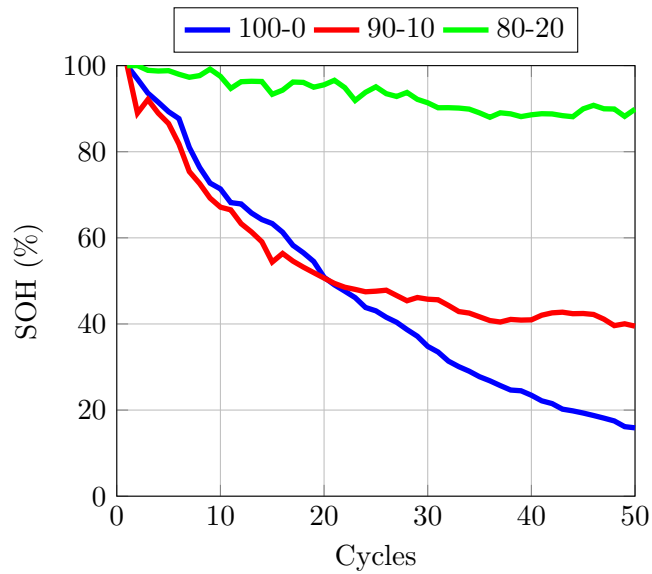


Figure 23: Capacity degradation in cycle aging tests.

DODs corresponds to a greater degradation of the battery even if the 80-20 curve differs too much from the degradation obtained with the other two tests, so it was decided not to consider it in the model calibration. In any case, these curves are representative only of the type of battery tested in this study since, in general, the degradation curves of commercial batteries initially are approximate to straight lines and have cycles of much longer life [21]. These results will be the calibration inputs of the model described in the next chapter.

3 Li-ion Cells Modelling and Simulation in GT-AutoLion

3.1 GT-AutoLion

GT-AutoLion, included in the GT-SUITE simulation software developed by Gamma Technologies, is the industry-leading Lithium-ion battery simulation software used by cell designers and OEMs to predict performance, degradation, and safety for any Lithium-ion cell. It predictively models the electrochemical processes within Lithium-ion cells using a fast and reliable, electrochemical, physics-based approach. The software can be used to predict how various Li-ion chemistries and cell designs will perform before Li-ion cells are prototyped or even available for testing. With GT-AutoLion, a Li-ion battery's performance can be predicted under any load, including constant current and more dynamic loads. The software uses the phisio-chemical Pseudo-2D model pioneered by Doyle, Fuller, and Newman to predict performance and includes a comprehensive electrochemical materials database, reducing the burden for laboratory testing of electrochemical properties. Also it is able to predict how Lithium-ion cells of any chemistry will degrade in any use case, including calendar aging, cycle aging, and mixed aging scenarios. It includes an extensive list of available Li-ion degradation mechanisms, such as: active material cracking, SEI and cathodic film growth, and Lithium-plating. These mechanisms enable users to predict not only capacity fade, but also resistance growth of a Li-ion cell as it ages. These models can be used to reduce testing time and cost, predict how batteries age in real-world scenarios, predict how aged batteries affect system performance, and calibrate and optimize fast charging strategies.

3.2 Lithium-ion battery model set-up

3.2.1 Model terminology

Before starting to describe the equations that are used in the model to describe the electrochemical mechanisms that take place inside the battery, it is necessary to introduce the variables involved:

- x : Distance in the thru-plane direction.
- r : Particle radius.
- t : Time.
- σ_s : Solid phase conductivity.
- Φ_s : Solid phase potential.
- Φ_e : Liquid phase potential.

- a_{dl} : Specific interfacial area.
- C : specific capacitance.
- j^{Li} : reaction current of Li.
- κ^{eff} : Electrolyte effective ionic conductivity.
- κ_D^{eff} : Effective diffusional conductivity.
- c_e : Li-ions (Li^+) concentration in the electrolyte-phase.
- c_s : Li-ions (Li^+) concentration in the solid-phase.
- $C_{s,e}$: Solid surface concentration.
- ϵ : Porosity.
- D_e^{eff} : Electrolyte phase Li Diffusion coefficient.
- t_+^0 : transference number.
- F : Faraday’s constant.

3.2.2 Theory behind the model

As already mentioned, GT-AutoLion uses the “Pseudo 2D” (P2D) electrochemical model for Lithium-ion (Li-ion) batteries based on the work of John Newman. The P2D model, discretize the Lithium-ion cell’s governing equations using the finite control volume approach, as pictured in Figure 4. In the P2D model, the Cathode, Separator, and Anode are discretized in the “thickness” direction. In each finite control volume of the Cathode and Separator, there is one spherical representation of active material, each of which are discretized in constant volumes in the radial direction. In Figure 24, the cathode and anode are shown to have 4 elements, the separator 3, and 6 elements in each of the active materials. Much of the theory and equations shown have been taken from the GT AutoLion guide and another study on electrochemical and thermal modeling of Li-ion battery carried out by Hosseinzadeh, E. Marco, J. Jennings, to which it’s necessary to refer for more completeness [22, 23].

The electrode is considered as a superposition of two phases, a solid electrode phase and an electrolyte phase. At the interface of this two phases the electro-chemical reaction takes place. The potential of these two phases can be described using the law of conservation of charge, in particular Ohm’s law becomes respectively:

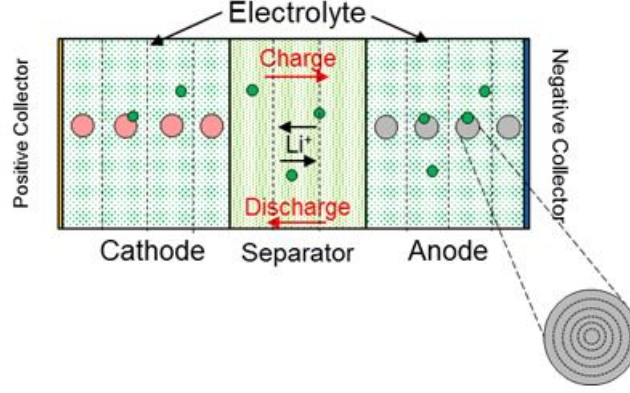


Figure 24: Cross-Sectional representation of Pseudo-2D model of a Lithium-ion cell.

- Solid phase:

$$\frac{\partial}{\partial x} (\sigma_s^{eff} \frac{\partial \Phi_s}{\partial x}) - j^{Li} - a_{dl} C \frac{\partial (\Phi_s - \Phi_e)}{\partial t} = 0 \quad (7)$$

At the electrode/current collector interface, the charge flux represents the external current, as expressed by:

$$BC_s : -\sigma_s^{eff} \frac{\partial \Phi_s}{\partial x} \Big|_{x=0} = -\sigma_s^{eff} \frac{\partial \Phi_s}{\partial x} \Big|_{x=L_{an}+L_{sep}+L_{cat}} = \frac{I}{A} \quad (8)$$

Also, there is no charge flux at the electrode/separator interface as stated below:

$$BC_s : \frac{\partial \Phi_s}{\partial x} \Big|_{x=L_{an}} = \frac{\partial \Phi_s}{\partial x} \Big|_{x=L_{an}+L_{sep}} = 0 \quad (9)$$

- Liquid electrolyte phase:

$$\frac{\partial}{\partial x} (\kappa^{eff} \frac{\partial \Phi_s}{\partial x}) + \frac{\partial}{\partial x} (\kappa_d^{eff} \frac{\partial \ln(c_e)}{\partial x}) + j^{li} + a_{dl} C \frac{\partial (\Phi_s - \Phi_e)}{\partial t} = 0 \quad (10)$$

A zero gradient boundary condition is imposed at the electrode/current collector interfaces:

$$BC_s : \frac{\partial \Phi_e}{\partial x} \Big|_{x=0} = \frac{\partial \Phi_e}{\partial x} \Big|_{x=L_{an}+L_{sep}+L_{cat}} = 0 \quad (11)$$

In the equation 7 and 10, the reaction current density and the double layer capacitance appears with opposite sign to guarantee the electroneutrality

on both a local and global basis. The electrical double layer (EDL) is a structure that appears on the surface of an object when it is exposed to a fluid. The EDL refers to two parallel layers of charge surrounding the object. The first layer, the surface charge (either positive or negative), consists of ions adsorbed onto the object due to chemical interactions. The second layer is composed of ions attracted to the surface charge via the Coulomb force, electrically screening the first layer. This second layer is loosely associated with the object. It is made of free ions that move in the fluid under the influence of electric attraction and thermal motion rather than being firmly anchored. It is thus called the "diffuse layer". Since it is schematized as a series of two capacitors, the dynamic effect on the potential of the two phases occurs mainly in the case of current pulses of the order of milliseconds, otherwise it is negligible (as in this study). The effective diffusional conductivity (κ_D^{eff}) is described by concentrated solution theory:

$$\kappa_D^{eff} = \frac{2RT\kappa^{eff}}{F}(t_+^0 - 1)\left(1 + \frac{d\ln f_{\pm}}{d\ln c_e}\right) \quad (12)$$

As the lithium ion concentration changes the intercalation/deintercalation processes within the solid phase, it is necessary to apply a mass conservation law inside the cell through Fick's second law. The distribution of Li in the spherical particles located in each control volume of the electrodes is predicted as:

- Solid phase:

$$\frac{\partial c_s}{\partial t} = \frac{1}{r^2} \frac{\partial}{\partial r} \left(D_s r^2 \frac{\partial c_s}{\partial r} \right) \quad (13)$$

No species source exists at the centre of the electrode particles, hence the boundary condition is defined as follows:

$$BC_s : \left. \frac{\partial c_s}{\partial r} \right|_{r=0} = 0; -D_s \left. \frac{\partial c_s}{\partial r} \right|_{r=R_s} = \frac{j^{Li}}{a_s F} \quad (14)$$

- Liquid electrolyte phase:

$$\frac{\partial}{\partial t}(\epsilon c_e) = \frac{\partial}{\partial x} \left(D_e^{eff} \frac{\partial c_e}{\partial x} \right) + \frac{1 - t_+^0}{F} j^{Li} \quad (15)$$

Lithium cannot diffuse through the current collectors, as set by the following boundary condition:

$$BC_s : \left. \frac{\partial c_e}{\partial x} \right|_{x=0} = \left. \frac{\partial c_e}{\partial x} \right|_{x=L_{an} + L_{sep} + L_{cat}} = 0 \quad (16)$$

At the interface of the solid and liquid phases the electrochemical reaction takes place. This reaction is described by the Butler-Volmer equation that express the volumetric intercalation reaction current of Li in the given electrode as:

$$j^{Li} = a_s i_0 \left\{ \exp \left[\frac{\alpha_{an} F}{R_u T} \left(\eta - \frac{R_f}{a_s} j^{Li} \right) \right] - \exp \left[\frac{\alpha_{cat} F}{R_u T} \left(\eta - \frac{R_f}{a_s} j^{Li} \right) \right] \right\} \quad (17)$$

Where a_s is the interfacial area between the two phases, i.e., the solid active material and the liquid electrolyte. The interfacial area can be calculated by treating the solid phase as a collection of uniform spheres, as displayed by the following equation:

$$a_s = \frac{3\epsilon_s}{r_p} = \frac{1 - \epsilon_e - \epsilon_f}{r_p} \quad (18)$$

Where ϵ_f is the porosity (volume fraction) of the fillers. η is defined as the difference between the solid and liquid phase potentials, minus the open-circuit potential of the solid, that is $\eta = \Phi_s - \Phi_e - U$. R_f is the electronic resistance of the surface film layer at the negative and positive electrode. While the exchange current density of the intercalation reaction (based on reaction surface area) i_0 , exhibits modest dependency on electrolyte and solid surface concentrations, because:

$$i_0 = k_i (c_e)^{a_s} (C_{s,max} - C_{s,e})^{\alpha_a} (C_{s,e})^{\alpha_e} \quad (19)$$

where k_i is the reaction rate which is temperature dependent. α is a dimensionless parameter, called the symmetry factor and defines the ratio between oxidation and reduction.

The partial differential equations 7,10,13,15 are integrated through the intercalation current density (j^{Li}) via the Butler-Volmer equation which defines cell electrochemical kinetics.

During the use of the battery, there is an internal generation of heat due to the reaction and additional losses (overpotential) which can lead to an increase in temperature. A lumped energy conservation model is applied to correlate the cell temperature (T) evolution to the generated heat inside the cell and the convective dissipated heat to the ambient as:

$$\frac{d(\rho c_p T)}{dt} = -h A_s (T - T_{amb}) + Q_{gen} \quad (20)$$

where h is the heat transfer coefficient, T_{amb} is the cooling medium temperature, A_s is the cell outer surface area, and Q_{gen} is the total heat generated within the cell. It is important to specify that the cell physico-chemical parameters ($\psi = D_s, D_e$ and i_0) have temperature dependency defined by Arrhenius's law as:

$$\psi = \psi_{ref} \exp \left[\frac{E_{act}}{R} \left(\frac{1}{T_{ref}} - \frac{1}{T} \right) \right] \quad (21)$$

Where ψ_{ref} is the parameter's value at the reference temperature T_{ref} and E_{act} is the activation energy which controls the temperature sensitivity of the given parameter.

3.2.3 Overpotential

As already introduced in the chapter 1.3, the battery voltage differs from that of OCV due to some losses called overpotential. Once the equations that regulate the electrochemistry of the cell have been introduced, it is easy to highlight the parameters on which these losses depend. The activation (or kinetic) overpotential is described by the Botler – Volmer equation (equation 17) which in fact has an exponential trend (exactly like the initial voltage drop) and can be adjusted through the exchange current density i_0 . The ohmic overpotential originates from the migration of ions inside the electrolyte, the resistivity of the current collectors and the electrodes, as well as the contact resistance between the electrodes and the current collectors. The contact resistance (R_c) between the electrodes and the current collectors is commonly used for tuning the ohmic resistance to obtain a good voltage match between the simulation and experimental values in the mid-SOC range of the voltage curve [24]. Therefore, the contact resistance is introduced into the voltage equation as:

$$V = \Phi_s(x = L_{cell}) - \Phi_s(x = 0) - \frac{R_c}{A} I \quad (22)$$

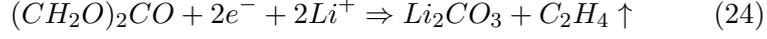
Where V is the cell voltage, A is the electrode plate area, and I is the applied current. The last overpotential, that of diffusion responsible for the final drop in the voltage curve (figure 7), is described by the Fick equation for the solid and liquid phase (equations 13,15) and is adjustable through the respective diffusion coefficients D_s and D_e . In most cases the effect of the diffusivity of the solid phase (in particular the anode) is the most relevant but the choice depends on the materials used for the electrodes, the electrolyte and the design of the battery [25].

3.2.4 Ageing theory

As already mentioned, the main degradation phenomena are: The growth of the SEI / CEI layer at the anode and cathode, the loss of active material and the plating of lithium.

- Anode SEI layer growth: In a graphitic anode, a SEI layer forms during the formation cycle and grows in subsequent cycling due to low equilibrium potential of lithiated graphite. Many studies have shown that the reason for this growth is the reaction between ethylene carbonate and lithium ions [22].





From the reaction of ethylene carbonate with lithium ions there is mainly lithium alkyl carbonate ($(CH_2OCO_2Li)_2$) and little formation of lithium carbonate (Li_2CO_3), therefore only the equation 23 will be modeled. Therefore, two moles of Li^+ and two moles of electrons are being consumed, which reduces the columbic efficiency of the system with the following kinetic equations:

$$j_{sei} = a_s i_{0,SEI} \exp \left[\frac{\alpha_{c,SEI} F}{R_u T} (\Phi_s - \Phi_e - U_{SEI} - \frac{R_{SEI}}{a_s} j^{Li}) \right] \quad (25)$$

Where j_{SEI} is the side reaction current density (based on reaction surface area), U_{SEI} is the equilibrium potential for the first chemical reaction, j^{Li} is the total current density of both lithium intercalation and side reactions and R_{SEI} is the resistance of the SEI layer. The exchange current density of the side reaction ($i_{0,SEI}$) depend on EC concentration at the reaction surface. Due to the creation of a side reaction at the interface of the active material particle and the SEI layer, the bulk EC has to diffuse through the porous SEI layer to reach the reaction site, so the Fick law for the EC diffusion can be written:

$$\frac{\partial c_{EC}}{\partial t} = D_{EC}^{eff} \frac{\partial^2 c_{EC}}{\partial r^2} \quad (26)$$

The EC effective diffusivity accounts for the torturous path in the SEI and is related to SEI layer porosity (ϵ_{SEI}) and EC diffusivity in the bulk solution by the following Bruggeman relationship, where n is the Bruggeman exponent:

$$D_{EC}^{eff} = D_{EC} (\epsilon_{SEI})^n \quad (27)$$

By solving the above equations, the growth rate of the SEI layer thickness (can be calculated as:

$$\frac{d\lambda_{SEI}}{dx} = - \frac{i_{s,AMSEI}}{2F\rho_{SEI}} \quad (28)$$

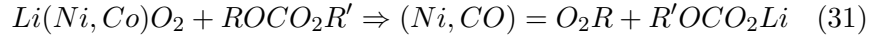
Where λ_{SEI} and ρ_{SEI} are the molecular weight and density of the SEI layer, respectively. The resistance of the SEI layer can be calculated by:

$$R_{SEI} = \frac{\lambda_{SEI}}{\kappa_{SEI}^{eff}} \quad (29)$$

κ_{SEI}^{eff} is the effective conductivity of the electrolyte through the porous SEI layer, also this parameter, like the effective diffusivity of the EC, is related to the inherent conductivity of the electrolyte via the standard Bruggeman relationship:

$$\kappa_{SEI}^{eff} = \kappa_{SEI} (\epsilon_{SEI})^n \quad (30)$$

- Cathode film growth: Most cathode materials have a high equilibrium potential that is beyond the stable window for typical electrolyte solvents. Thus, the lithium ion intercalation processes are often preceded by the formation of a surface film on the active cathode material surface. For lithium nickel cobalt oxides, the surface film is mainly composed of polycarbonates, LiF, and oxide reduction products. The oxide film growth can be considered to grow from the following reaction, where R is a radical:



The oxide film formation and growth in the cathode via the above reaction is considered by using the following rate equation:

$$J_{s,C} = k_{s,C} C_{EC,s} C_{Li_x(Ni,CO)O_2} \quad (32)$$

Here, $J_{s,C}$ is the side reaction rate per surface area (mol/m^2), $k_{s,C}$ is the reaction rate coefficient ($m^4/mol/s$), $C_{EC,s}$ is the EC concentration at the surface of the active material particle, and $C_{Li_x(Ni,CO)O_2}$ is the cathode material molar concentration. The loss of active cathode material due to the above reaction is given by:

$$\frac{d\epsilon_{Li(Ni,Co)O_2}}{dx} = -\frac{a_s J_{s,C}}{C_{Li(Ni,Co)O_2}} \quad (33)$$

$\epsilon_{Li(Ni,Co)O_2}$ is the active material volume fraction in the electrode. This loss of active material in the cathode leads to capacity fade. As for the SIX layer, the growth of the cathode film is modeled with a mass balance:

$$\frac{d\lambda_{film}}{dt} = J_{s,C} \frac{M_{film}}{\rho_{film}} \quad (34)$$

Where, again, ρ_{film} represents the cathode oxide film growth, M_{film} represents the molecular weight of the film, and ρ_{film} represents the density of the film.

- Cathode/Anode active material isolation: The intercalation and deintercalation of Li in the structure of active materials leads to mechanical stress and induces cracking and structural damage that more or less quickly lead to the loss of active material during cycling. This loss can occur in the anode, in the cathode or in both and depends on the structure and materials of the latter. Since the active material (AM) isolation is a consequence of the lithium intercalation process, it's possible to relate the isolation rate to intercalation current such that:

$$\frac{d\epsilon_{AM}}{dt} = -k(T) |j^{Li}| \quad (35)$$

where ϵ_{AM} is the volume fraction of active material, $k(T)$ is a temperature-dependent fitting parameter, and j^{Li} is always the intercalation current.

- **Lithium plating:** If the potential in a finite volume of the anode falls below zero volts, cycling lithium (Li^+) will react with electrons (e^-) to form lithium metal. This lithium metal is deposited into the anode, lowering the porosity of the anode. This effect is taken into account together with the growth of the SEI layer:

$$\frac{d\epsilon}{dt} = -a_s \frac{d(\lambda_{SEI} + \lambda_{Lip})}{dt} \quad (36)$$

where ϵ represents porosity, a_s represents the volume specific reaction surface area, and $\lambda_{SEI} + \lambda_{Lip}$ represents the growth of the surface film thickness. As the side reaction proceeds, there is a decrease in the available active surface area of the negative electrode because of the clogging of the particle surface due to the side reaction product, which is represented by:

$$a_s = a_{s,0} \left[1 - \left(\frac{\epsilon_0 - \epsilon}{\epsilon_0} \right) \zeta \right] \quad (37)$$

Where ζ is the morphology factor of the side reactions product. Its value is between 0 and 1 and a $\zeta = 0$ means that the side reaction products instantaneously spread over the whole reaction surface and blocks the reaction completely. While $\zeta = 1$, means that the side reaction products spread over the reaction surface laterally.

The anode/cathode layers growth with lithium plating are schematized in the figure 25.

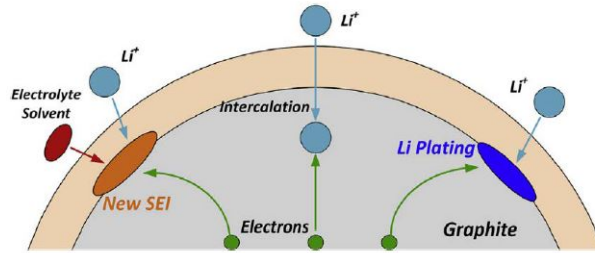


Figure 25: SEI growth and Li plating degradation phenomena.

3.3 Model Calibration and Validation on Discharge Tests

The process of calibrating the model on the experimental discharge curves is divided into two main parts.

1. **Static calibration:** Where, using the curve with the lowest current (C/20), an attempt is made to calibrate those characteristic parameters of the battery that do not depend on the current. This method in fact provides the hypothesis that the battery is in OCV continuously during its discharge, and it's also called *OCV calibration*.
2. **Dynamic calibration:** Where, the highest C-RATE curves are used to calibrate those parameters that depend on the current and affect the overpotentials, therefore on the kinetic, resistive and diffusive effects that occur inside the battery.

These procedure are in turn divided into a first step, called pre-optimization, in which a sensitive analysis is carried out to find the upper and lower limits of the parameters that affect the performance of the cell. A second step that is the real optimization, in which a genetic algorithm is used that exploits a multi-objective weighted sum approach to find the best parameter values, between the ranges found in the previous step, that reflect the performance of the batteries used in the experimental tests. To evaluate the accuracy and good fit of the model, two other post-optimization calculated indices are used [24]:

- The relative root mean square error (RRMSE) which is an index used to evaluate the model accuracy. A lower value indicates a more accurate model.

$$RRMSE_V(\%) = \frac{RMS_V}{V_{avg}} \cdot 100 \quad (38)$$

- The R-squared that is a goodness of fit index to assess how the simulated results match the experimental ones. A value as close to one as possible indicates a very appropriate fitting.

$$R^2 = 1 - \frac{\sum(V_{i,exp} - V_{i,sim})^2}{\sum(V_{i,exp} - V_{i,avg})^2} \quad (39)$$

3.3.1 Model creation

The model created for static and dynamic calibration on experimental tests is shown in figure 26. The analysis of each single block will be carried out below.

- **Battery block:** The first very important thing to include in the battery block is its geometry. In the case under study it is a coin cell with

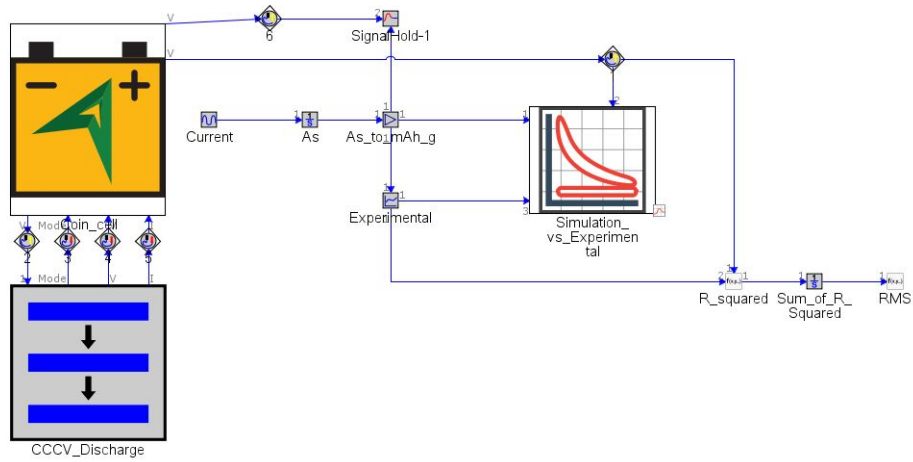


Figure 26: Calibration model on GT-AutoLion.

standard assembly and geometry shown in table 2. Subsequently, the active materials that make up the anode and the cathode must be chosen, in the case under study respectively Graphite and NMC622. The mass fractions of active material are known from previous studies

Attribute	Unit	Object Value
Formula		
Active Material #1		Graphite...
Active Material #1 Mass Fraction	See Case...	[MASSFRAC_AN]...
<input type="checkbox"/> Active Material #2		
Conductive Agent Density	g/cm ³	1.95...
Conductive Agent Mass Fraction	fraction	0.078...
Binder Density	g/cm ³	1.77...
Binder Mass Fraction	fraction	=1-[MASSFRAC_AN]...
Additive Density	g/cm ³	ign...
Additive Mass Fraction	fraction	0...
Anode Coating		
<input checked="" type="radio"/> N/P Ratio	See Case...	[NoverP]...
<input type="radio"/> Capacity Loading	mA/h/cm ²	
<input type="radio"/> Porosity	A-h	
<input type="radio"/> Capacity	A-h	
Conductivity		
Conductivity	S/m	1E2...
Contact Resistance (@ Foil/Anode Interface)	See Case...	[Contact_Resistance]...
Terminal to Foil Resistance	Ohm	ign...
Mechanical Deformation		
Stress-Strain Relationship		ign...

Attribute	Unit	Object Value
Formula		
Active Material #1		NMC622...
Active Material #1 Mass Fraction	See Case...	[MASSFRAC_CAT]...
<input type="checkbox"/> Active Material #2		
Conductive Agent Density	g/cm ³	1.95...
Conductive Agent Mass Fraction	fraction	=1-[MASSFRAC_CA]...
Binder Density	g/cm ³	1.77...
Binder Mass Fraction	fraction	0.018...
Additive Density	g/cm ³	ign...
Additive Mass Fraction	fraction	0...
Cathode Coating		
<input checked="" type="radio"/> Capacity Loading	See Case...	[CapLoading]...
<input type="radio"/> Porosity	A-h	
<input type="radio"/> Capacity	A-h	
Conductivity		
Conductivity	S/m	3.8...
Contact Resistance (@ Foil/Cathode Interface)	See Case...	[Contact_Resistance]...
Terminal to Foil Resistance	Ohm	ign...
Mechanical Deformation		
Stress-Strain Relationship		ign...

(a) Anode template in GT-AutoLion. (b) Cathode template in GT-AutoLion..

Figure 27: Compilation of active material templates in GT-AutoLion modeling software.

carried out on the materials used for the coin cells and are worth 90% for graphite and 95% for NMC622. The next step is to fill in the assembly part with the electrode materials (copper and aluminum), the separator and the electrolyte. Finally, it is possible to insert a thermal model for the internal generation of heat and the heat exchange with the external environment (equation 20) but it was assumed to be negligible as very low currents are used (max C/5) and the test at 45°C

it is at a controlled temperature in a ventilated environment so it can be assumed that it is equal to that of the coil. While for the tests at room temperature a temperature of 26°C was set.

- **Event Manager:** This block has the function of controlling the discharge of the battery. In particular, GT-AutoLion automatically terminates the simulation when the voltage of the experimental curve or the simulated one drops below the cut-off value, equal to 2.5V. With this block a constant current discharge between 4.3V and 2.5V is set and then a fictitious constant voltage discharge is imposed in order to allow both curves to reach the cut-off voltage.
- **Monitor:** The function of this block is to plot the experimental data against the simulated ones, the maximum and minimum values of the axes with their respective names are set. The data to be plotted comes from the battery pack for the simulated voltage while the simulated capacity is calculated as the integral of the current (preset for the various C-RATEs) and subsequently divided by the mass of active material of the NMC622 in order to obtain a specific capacity mAh/g . It's important to specify that the various coin-cells used had a different weight of active material (of a few milligrams), so the weight of NMC622 of the battery to be modeled was assumed to be equal to the average of the NMC622 weights of the batteries at ambient temperature (test 1 and 3) and at 45°C (test 1 and 2) from which the mean discharge curves were calculated (31.4 mg). The experimental data comes from a pre-set table.
- **Mathematical blocks:** These are used to first calculate the difference of the squares between the curves and subsequently integrate it in the simulation time to obtain the root mean square value (RMS) between the simulated and experimental curves. The latter is the objective function that we want to minimize using the case sweep optimization.

$$Minimize \left(RMS = \sqrt{\frac{1}{t} \int_0^t (V_{exp} - V_{sim})^2 dt} \right) \quad (40)$$

This optimization is carried out through GT-AutoLion's "Design Optimizer" tool, wich goal is to find an optimal solution that provides the best fit between the experimental and predicted values for the given optimization objective for all the tests considered, that are C/20, C/10 and C/5 curves at ambient temperature and 45°C.

The Design Optimizer uses a genetic algorithm to find the optimal parameter sets, it is a heuristic algorithm that allows to evaluate different

starting solutions (as if they were different biological individuals) and that recombining them (similarly to sexual biological reproduction) and introducing elements of disorder (similarly to random genetic mutations) produce new solutions (new individuals) which are evaluated by choosing the best ones (environmental selection) in an attempt to converge towards "best" solutions. Given the inherently random nature of the genetic algorithm, there is no a priori way of knowing whether it will actually be able to find an acceptable solution to the problem under consideration.

3.3.2 Static calibration

Once the calibration procedure is understood, it is very important to introduce the static calibration parameters:

- Cathode capacity loading ($Loading^{Ca}$) (mAh/cm^2): It is the amount of charge per unit area present at the cathode. It is an important parameter for the energy-power balance of the cell and is influenced by the amount of active material. If not a lot of material is placed in the cathode, the cell will have a small amount of capacity or energy storage capability but will be able to allow for high C-rates. If a lot of material is placed in the cathode, the cell will have a large amount of capacity or energy storage capability but will not be able to allow for high C-rates. It was estimated by dividing the charge capacity of the first cycle at C/20 by the area of the NMC622 disk.
- N/P (-): It is the ratio between the capacity loading of the anode and that of the cathode.

$$\frac{N}{P} = \frac{\text{Anode capacity loading (mAh/g)}}{\text{Cathode capacity loading (mAh/g)}} \quad (41)$$

- NMC622 and Graphite First charge capacity (FCC^{Ca} and FCC^{An}) (mAh/g): During the initial formation and first charge and discharge cycles, a certain amount of lithium, or capacity, is lost for the formation of the initial Solid Electrolyte interface (SEI) layer. The first charge capacity, is the amount of lithium accepted, either the graphite and NMC 622, during the initial lithiation of the material (first charge) per unit of active material mass. The FCC of NMC622 was estimated by dividing the capacity of the first charge cycle at C/20 by the mass of NMC622 weighted during battery assembly.
- NMC622 and Graphite first discharge capacity (FDC^{Ca} and FDC^{An}) (mAh/g): Is the amount of lithium returned in the cathode and anode materials, after initial lithiation per unit of active material mass. The difference between FCC and FDC represents the irreversible capacity of the cathode and anode respectively.

- Maximum voltage NMC622 (U_{max}^{Ca})(V): is the maximum open circuit potential of the NMC622.

The static calibration process was carried out using the curves at C/20 at room temperature (26°C) and at a temperature of 45°C at the same time, assuming constant temperature conditions. The estimation of the other parameters was carried out through a sensitive analysis, the already anticipated pre-calibration part, through which the initial values with the upper and lower limits were obtained. These values have been inserted into the design optimizer using the mean value of the RMSs calculated with the equation 40 for the curve at room temperature and that at 45°C as objective function adding a constrain on the simulated capacity which must be $\pm 5\%$ of the experimental one. The optimization results are summarized in table 6.

Table 6: Starting, boundaries and design value for the static calibration parameters.

Parameter	Unit	Starting value	Boundaries	Final value
$Loading^{Ca}$	mAh/cm^2	3.35	3.15÷3.45	3.362
N/P	-	1.3	1.2÷1.35	1.344
FCC^{Ca}	mAh/g	180	170÷190	175.01
FDC^{Ca}	mAh/g	165	160÷170	163.9
FCC^{An}	mAh/g	370	365÷375	374.5
FDC^{An}	mAh/g	345	340÷350	348.8
U_{max}^{Ca}	V	4.40	4.35÷4.45	4.365

To have a clearer view, it is possible to see the trends of the simulated and experimental curves used to calculate the average curve useful for calibration in figure 28.

The calibration of the set of parameters has led to a good fitting in the activation and ohmic part of the characteristic curve while the precision in the final diffusive part for the simulation at room temperature worsens while it is better but not perfect for the 45 ° C curve. It is important to specify that the average curve is calculated by discretizing the axis of the specific capacity and by averaging the voltages (i.e. vertically), so it shouldn't be expected a curve that lies perfectly in the middle as an index of good fitting. In any case, the statistical values previously introduced to evaluate the results of the model are shown in the table below. These parameters also confirm the best precision and fitting on the 45°C curve. The discrepancies are due to the fact that curves at C/20 at 45°C showed a higher cathode FCC and FDC and a higher capacity loading than the battery at room temperature, leading the optimizer to find a trade-off that penalized the accuracy of the simulation.

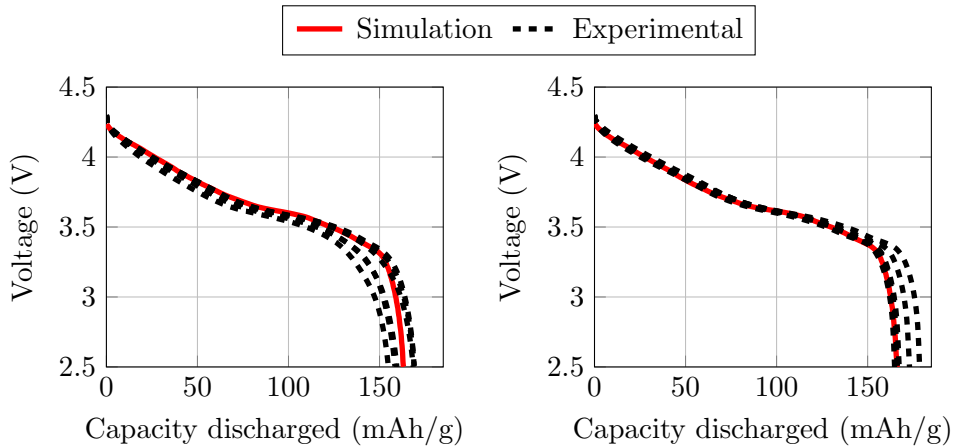


Figure 28: C/20 simulation discharge curves at ambient temperature (left) and 45°C (right) versus all experimental curves considered for the calculation of the mean one.

Table 7: Statistical parameters to evaluate the results of the static calibration.

Case	RRMSE	R ²
C/20 (26°C)	1.95%	0.957
C/20 (45°C)	1.21%	0.975

3.3.3 Dynamic calibration

Once the static parameter sets that define the cell balance have been found, it is also necessary to calibrate the parameters that depend on the current and, as already seen, greatly affect the discharges at larger currents. Once again, before going into the analysis of the results, it is necessary to introduce these parameter already announced in chapter 3.2.3.

- Cathode exchange current density (i_0) (A/m^2): It appears in the Butler-Volmer equation (equation 17) and is the current in the absence of net electrolysis and at zero overpotential. Exchange current densities reflect intrinsic rates of electron transfer between an analyte and the electrode providing insights into the structure and bonding. The exchange current density depends critically on the nature of the electrode, not only its structure, but also physical parameters. The nature of the electroactive species (the analyte) in the solution also critically affects the exchange current densities, both the reduced and oxidized form. For these reasons in the assembled coin-cell the effect of NMC622 is prevalent. This parameter has a greater influence on the initial drop of the characteristic curve, a lower value of i_0 is reflected

in a lower voltage with the same discharge capacity.

- Contact resistance (R_c) ($mOhm \cdot m^2$): Is the contact resistance between the electrodes and the collectors, it is a parameter that influences the trend of the curve in the ohmic drop part and is supposed to be the same between cathode-copper and anode-aluminum.
- Graphite Diffusivity ($D_{s,an}$) (m^2/s): Is the diffusivity of the lithium ions inside the anode electrode, in this case graphite. As already seen, it appears in the conservation equation of Fick species (in the solid part) and has an influence, and has a great influence on the behavior of the characteristic curve in the high SOC part.
- NMC622 Diffusivity ($D_{s,ca}$) (m^2/s): Is the diffusivity of the lithium ions inside the cathode electrode, in this case NMC622. It is part of the Fick equation applied to the cathode (always in the solid part) and has an influence, albeit secondary to that of graphite, on the trend of the characteristic curve in the high SOC part.

The starting values of these parameters are those preset by the modeling software. In any case, for i_0 , D_{an} and D_{ca} a multiplicative coefficient of the database value is calibrated for which they will have no unit of measurement. Another important parameter on dynamic performance is the heat transfer coefficient h (W/m^2K) since as already discussed in the previous chapters, the dynamic parameters depend on the temperature. For this study it was decided to neglect it as the currents involved are small and through a sensitive study it has been demonstrated that it is ineffective from the point of view of simulations. The dynamic calibration procedure is carried out in the same way as the static one, considering as a case study the average curves at C/10 and C/5 of the tests at room temperature and controlled at 45°C. After a sensitive analysis in which the starting values and the optimization ranges are found, the parameters illustrated are inserted in the GT-AutoLion design optimizer tool, always setting a constrain on the simulated capacity which must be $\pm 5\%$ of the experimental one. As objective function the average of the RMS calculated for each case study is used. The dynamic optimization results are summarized in table 8. For clarity, the

Table 8: Starting, boundaries and design value for the dynamic calibration parameters.

Parameter	Unit	Starting value	Boundaries	Final value
i_0	–	0.3	0.2÷0.4	0.299
R_c	$mOhm \cdot m^2$	4.0	2.5÷5.5	3.007
$D_{s,an}$	–	0.045	0.03÷0.06	0.0444
$D_{s,ca}$	–	0.1	0.03÷0.3	0.0508

simulated and all experimental curves used to calculate the mean curve are shown in figure 29.

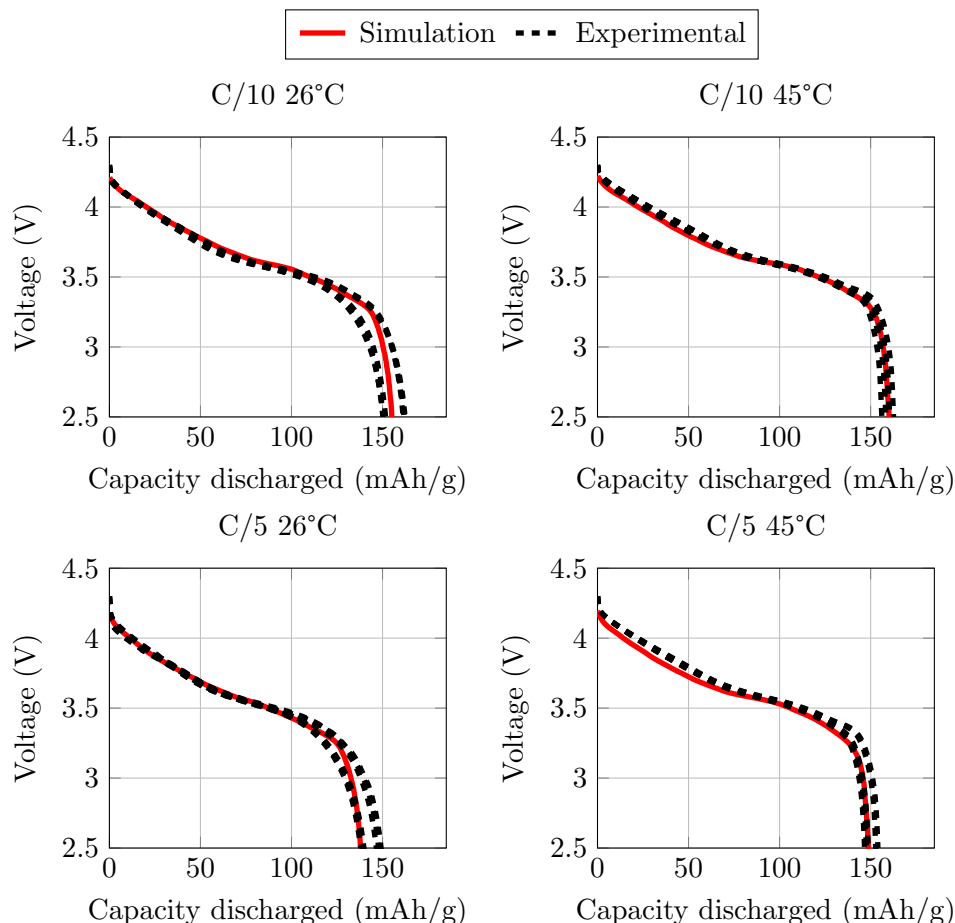


Figure 29: C/10 and C/5 simulation discharge curves at ambient temperature (left) and 45°C (right) versus all experimental curves considered for the calculation of the mean one.

A good fitting of the experimental curves was obtained for all cases. However a slight difference can be noted in the resistive section of the C/5 curve at 45°C. This is because the contact resistance is a function of the temperature which improves performance by reducing the ohmic overpotential (that is increased by the higher current), therefore the simulation at ambient temperature will have a greater sensitivity to the change of this parameter (but also of the others that have an analogical dependence on the temperature, equation 21) which involves a convergence to values that improve the fitting of these curves. In any case, this effect is only accentuated by the different tendency in that section of the experimental curves, while for the diffusive

section, analogous trends are obtained. To have an objective evaluation, the statistical parameters useful for evaluating the precision and fit of the model are shown in the table 9.

Table 9: Statistical parameters to evaluate the results of the dynamic calibration.

Case	RRMSE	R^2
C/10 (26°C)	1.20%	0.982
C/10 (45°C)	0.959%	0.987
C/5 (26°C)	1.29%	0.980
C/5 (45°C)	1.29%	0.974

The best fitting is obtained for the curve at C/10 at 45°C which, thanks to the lower current, has a less marked ohmic drop. In any case, the fitting and accuracy of the simulations are good for all experimental curves.

3.4 Model Calibration and Validation on Cycle Aging Tests

The degradation phenomena previously discussed are the basis for creating an aging model. It is important to summarize when these degradation phenomena occur [22]:

- The electrode film growth model leads to a loss of capacity even when the cell is in storage.
- The loss of active material model leads to a loss of capacity when current passes through the cell.
- The lithium plating model leads to a loss of capacity only in periods of recharging at high currents or recharging at low temperatures.

It is understood that in order to correctly calibrate all phenomena it is first necessary to calibrate the growth of the anode and cathode layers and then be in possession of calendar aging tests, where the battery is stored and the loss of capacity over time is monitored. Not being in possession of the results of these tests, an approach will be proposed where the model will be calibrated on the experimental results of cycle aging (figure 23) taking into account the effects of the growth of the anode and cathode films but mainly to calibrate the consequent degradation of the diffusivity of the electrolyte and the loss of anode and cathodic active material. Lithium plating, being that recharging occurs at currents of the order of C/10 and at ambient temperature, will be considered but will not be calibrated. All these degradation phenomena have been hypothesized to have an Arrhenius dependence on temperature (equation 21), for which the pre-exponential part

(ψ_{ref}) and the activation energy (E_{act}) will be considered in the calibration process and are summarized below.

- SEI layer growth reference value: ψ_{SEI}
- SEI layer growth activation energy (J/mol): E_{SEI}
- CEI layer growth reference value: ψ_{CEI} .
- CEI layer growth activation energy (J/mol): E_{CEI}
- EC diffusivity degradation reference value from graphite: $\psi_{EC,An}$
- EC diffusivity degradation from graphite activation energy (J/mol): $E_{EC,An}$
- EC diffusivity degradation reference value from NMC622: $\psi_{EC,Ca}$
- EC diffusivity degradation from NMC622 activation energy (J/mol): $E_{EC,Ca}$
- Anode active material isolation reference value: $\psi_{AMI,An}$
- node active material isolation activation energy (J/mol): $E_{AMI,Ca}$
- Cathode active material isolation reference value: $\psi_{AMI,An}$
- Cathode active material isolation activation energy (J/mol): $E_{AMI,Ca}$

Before proceeding with the optimization it is necessary to carry out a pre-calibration of these parameters to find the maximum and minimum ranges and the starting value. Subsequently it is possible to proceed with the optimization by setting as a constrain that the set of parameter values leads to a minimum number of cycles equal to 50, exactly as in the experimental case.

3.4.1 Model creation

The model created for the degradation phenomena calibration using the data from cycle aging tests is shown in figure 30. The analysis of each single block will be carried out below.

- **Battery block:** The battery pack is the same used for the characterization process and uses the optimal values of the static and dynamic calibration parameters obtained. The substantial difference is that in the active material section of the anode and cathode, the degradation phenomena previously introduced have been activated.

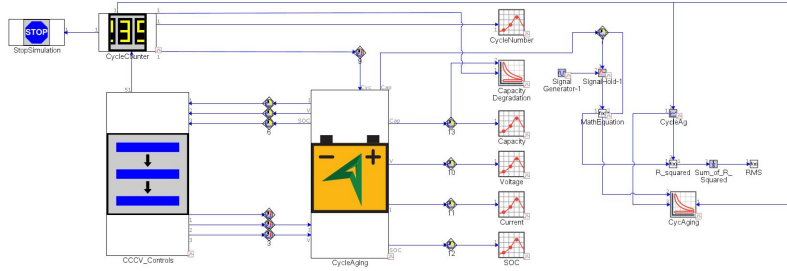


Figure 30: Calibration model for degradation phenomena.

Main		Degradation	
Attribute	Unit	Object Value	
Film Growth			
Initial Film Thickness	nm	5 ...	
Film Conductivity	S/m	AnodeFilmConductivity ...	
<input type="radio"/> No Film Growth			
Anode SEI Layer Growth			
EC Diffusivity	m^2/s	AnodeECDiff ...	
SEI Reaction Rate Coefficient		AnodeFilmGrowth ...	
SEI Equilibrium Potential	V	0.4 ...	
SEI Charge Transfer Coefficient		0.5 ...	
SEI Molecular Weight	g/mol	162 ...	
SEI Density	g/cm^3	1.69 ...	
SEI Porosity		0.05 ...	
<input type="radio"/> Cathode CEI Layer Growth			
Active Material Isolation			
<input checked="" type="checkbox"/> Active Material Isolation			
Isolation Rate		AnodeAMI ...	
Lithium Plating			
<input type="checkbox"/> Anode Lithium Plating			
Exchange Current Density	A/m^2	AnodeLPL ...	
Equilibrium Potential	V	0 ...	
Charge Transfer Coefficient		0.5 ...	
Morphology Factor		0.03 ...	

Figure 31: Example of configuration of the anodic template with degradation phenomena.

- **Event Manager:** This block is always used to check the charge and discharge of the battery pack. The maximum and minimum voltages are set between which to cycle the battery exactly as in the experimental test (table 5).
- **Cycle counter:** This block has the function of increasing the number of cycles each time the cell discharges and recharges between the two set voltage limits. Once the maximum cycle value has been reached (50) , the simulation is stopped.
- **Monitor:** These have the function of plotting some fundamental battery parameters such as capacity degradation, voltage, etc. against time or the number of cycles.
- **Mathematical blocks:** These are used to first calculate the difference of the squares between curves and subsequently integrate it in the number of cycles to obtain the root mean square value (RMS) between the simulated and experimental degradation curves (these are inserted through a signal generator that refers to the pre-set tables with the data). Again, the latter is the objective function to minimize using the case sweep optimization.

$$Minimize \left(\sqrt{\frac{1}{cycle} \int_0^{maxcycle} (SOH_{exp} - SOH_{sim})^2 dcycle} \right) \quad (42)$$

3.4.2 Model results

The results of the optimization process are shown in the table 10 together with the upper and lower boundary conditions. It's possible to notice that the optimization ranges are very wide, this is because it is not easy to pre-calibrate the degradation phenomena considering them together as the decrease of one could lead to the increase of the range of another. In any case, the results of the optimization are better represented in the figure 32 It can be seen how a more appropriate fitting is obtained in the 90-10 case, while in 100-0 it is possible to describe the trend but with a poorer fitting. The same statistical indices used for the characterization are shown in table 11. As already clear, the fitting and accuracy of the model on the case of cycle aging between SOC 90% -10% is higher. In any case, the results are worse than the battery characterization discussed in the previous chapter but they demonstrate how it is possible, using GT-AutoLion, to describe the degradation processes starting from an experimental basis although this is not very solid as they are not commercial batteries but coin-cells manually assembled.

Table 10: Starting, boundaries and design value for the cycle aging calibration parameters.

Parameter	Unit	Starting value	Boundaries	Final value
ψ_{SEI}	–	1E-13	1E-15÷1E-10	1.32E-12
E_{SEI}	<i>J/mol</i>	3E5	1E4÷1E6	3.13E5
ψ_{CEI}	–	1E-13	1E-15÷1E-10	2.40E-14
E_{CEI}	<i>J/mol</i>	3E5	1E4÷1E6	7.60E5
$\psi_{EC,An}$	–	1E-13	1E-15÷1E-10	1E-13
$E_{EC,An}$	<i>J/mol</i>	3E5	1E4÷1E6	6.12E5
$\psi_{EC,Ca}$	–	1E-12	1E-15÷1E-10	1E-12
$E_{EC,Ca}$	<i>J/mol</i>	1E4	1E3÷1E6	1E4
$\psi_{AMI,An}$	–	1E-13	1E-14÷1E-11	1E-13
$E_{AMI,An}$	<i>J/mol</i>	3E5	1E4÷1E6	6.45E5
$\psi_{AMI,Ca}$	–	1E-12	1E-15÷1E-11	6.70E-13
$E_{AMI,Ca}$	<i>J/mol</i>	1E4	1E3÷1E6	2.69E5

Table 11: Statistical parameters to evaluate the results of the cycle aging calibration.

Case	RRMSE	R^2
100-0	18.4%	0.882
90-10	5.64%	0.969

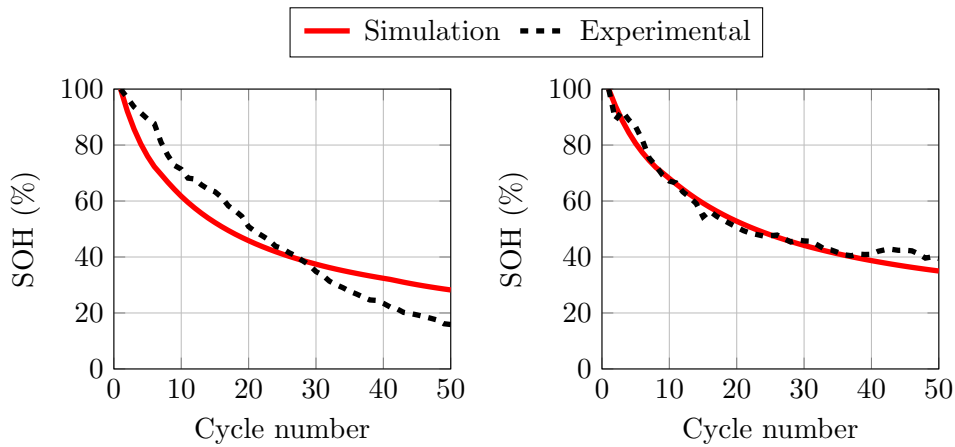


Figure 32: Results of the calibration of cycle aging between SOC 100-0 (left) and 90-10 (right).

3.5 GT-AutoLion Model Applications

3.5.1 Support to the cell design

Validating a methodology to characterize the battery in order to obtain a digital twin is useful not only to be able to predict the performance of the latter but it is certainly an aid in the design phase for companies and OEM's. In fact, it is possible to take advantage of GT-AutoLion to check which are the most influential parameters on battery performance and then carry out targeted interventions during manufacturing, these operations carried out on a virtual model allow to reduce experimental tests, saving money and time. For example, to improve performance it is necessary to reduce the size of the particles that make up the anode and the cathode but to understand which of the two it is convenient to act on and how the discharge curves change with the variation of this parameter, the digital model is of great help. Figure 33 shows how the increase in the particle size of NMC622 worsens the performance of the battery at each discharge capacity (and therefore SOC) having a more marked effect at high temperatures while the increase in graphite particles has an influence only at high SOC (in the diffusive part) and at low temperatures such as ambient ones, in conclusion it is better to keep the focus on the particle size of NMC622 for this type of coin-cell. Similar reasoning can be made about other design parameters such as the dimensions (diameter or thickness) of the electrodes or of the separator.

3.5.2 Support to the battery management

Another strong point of the application of the model is that after having also calibrated it on the phenomena of degradation, strategies can be developed

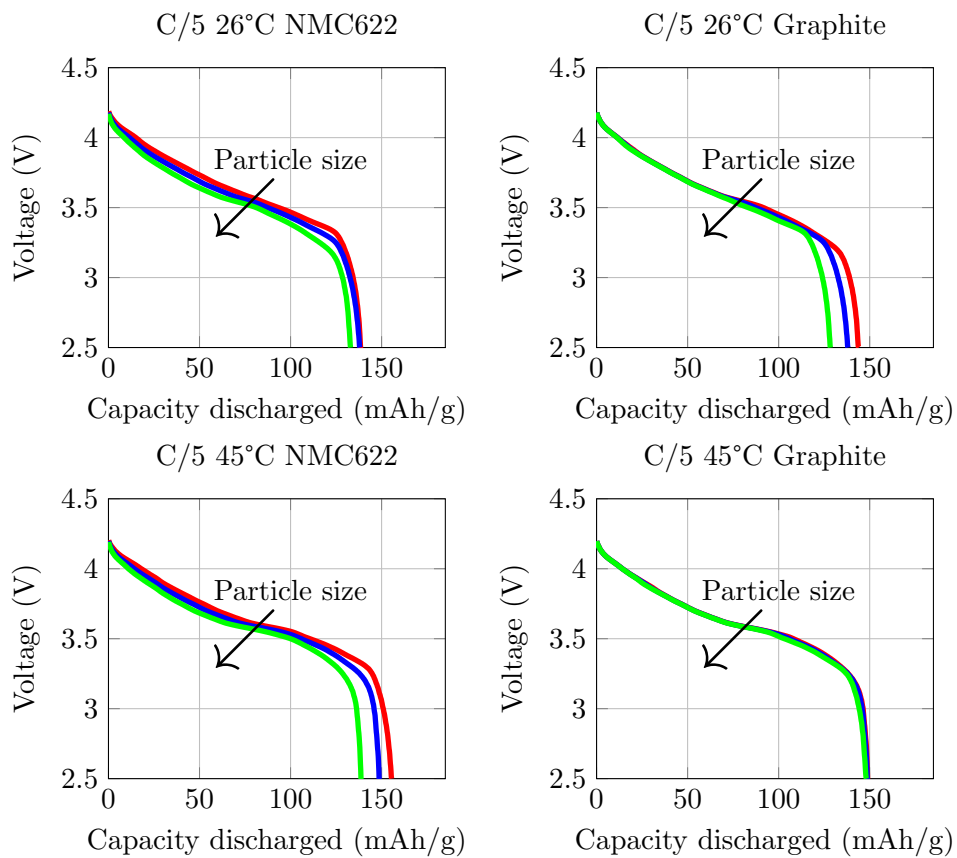


Figure 33: Sensitivity of the calibrated model at ambient temperature and 45°C (C/5 curves) to the variation in the diameter of the particles that make up the NMC622 (left) and graphite (right)

on battery management, that is, limit the charge and discharge between two SOCs or limit the charge or discharge current. These techniques can be very useful to increase the life of the batteries and, through the digital twin, it is possible to study which elements have the most influence on degradation. In figure 34, the trend of the simulated state of health of the coin-cell is

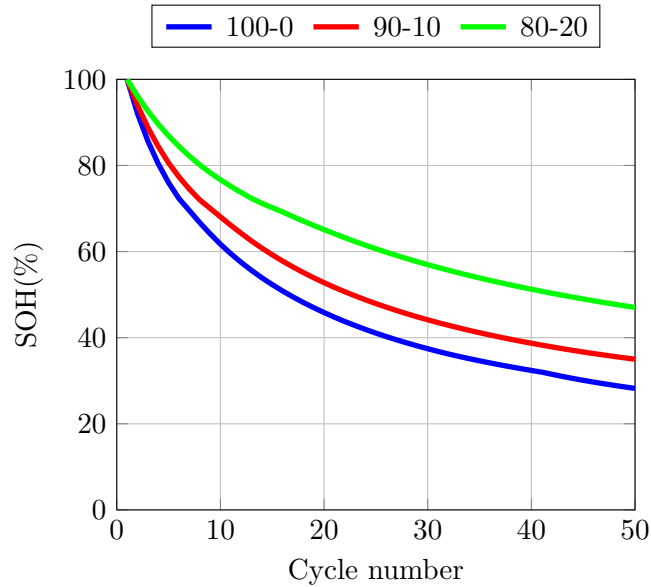


Figure 34: Simulated SOH at various DOD.

shown in function of various DOD in a cycle aging test in CC, obviously as already said, the lower the DOD, the lower the degradation.

3.5.3 Integration with other sub-system

Another important facet of GT-AutoLion is the possible integration of the calibrated battery model with other subsystems such as the temperature control system or even more in a vehicle model. Figure 35 shows, the GT-SUITE integrated model of an electric vehicle that uses a battery pack that can be calibrated with the methodology described in this study in order to simulate real performance.

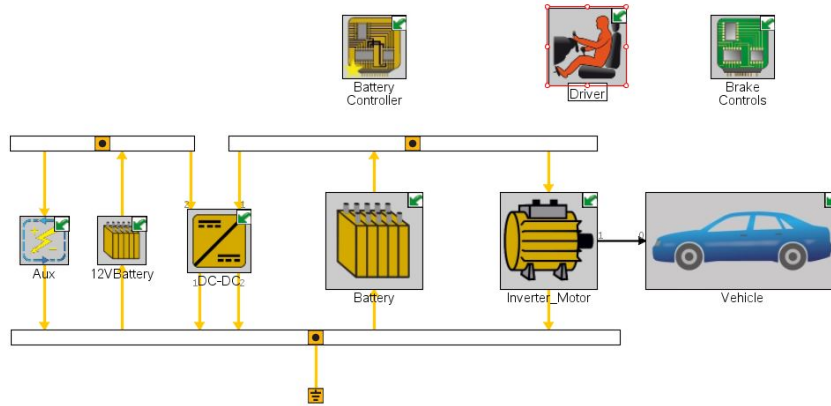


Figure 35: Model of a BEV created in GT-AutoLion.

4 Conclusion

The object of this work was the creation of a digital twin of a lithium ion coin-cell battery (Graphite-NMC622) which reflects the average discharge trends of various batteries created and tested in the DISAT laboratories of the Polytechnic of Turin and characterizes the degradation phenomena based on cycle aging experiments. This work is very timely as we are moving towards a decarbonisation of the transport sector which will lead to an increase in electric cars and consequently lithium-ion batteries in the market. The experimental characterization tests, carried out with the assembly and optimal geometries (defined as standard), were successful, bringing more tests to completion and therefore a good basis was obtained for the virtual characterization of the battery that it was decided to stop at the current of C/5 for reasons of performance of the coin-cells. The experimental characterization of the degradation phenomena was carried out through CC cycle aging tests between two different SOC_s (100%-0% and 90%-10%). The experimental basis is poor in order to describe all the degradation phenomena and calendar aging tests would have been needed, even at different temperatures, in order to have massive experimental data but it would require more time than that available for the study of this thesis. Despite this, the virtual model of the coin-cells on GT-AutoLion was created, carrying out the calibration based on the previous experimental tests both for the discharge characteristic curves and for the cycle aging tests, managing to obtain very precise and accurate results. Successful validation of the characterization procedure for creating the digital twin opens the door to many other applications: it can provide support to companies (OEM's) in the creation of batteries as the most influential design parameters on performance and therefore on efficiency can be verified by being able to carry out optimiza-

tion studies. GT-AutoLion can also be exploited by companies operating in the automotive sector as it is possible to integrate the digital twin of the characterized battery with other subsystems such as temperature control or even in a complete model of an electric vehicle. They can exploit it not only to verify the correct coupling with the other subsystems but they can also optimize the BMS, implementing charging/discharging and battery use modes in general that increase its life cycles. In conclusion, the characterization methodology coupled with the CAE simulations open a world, not yet fully explored, of potential to be exploited.

References

- [1] POWERTECH Engineering: Your Competent Partner for Powertrain Simulation and Development, <https://pwt-eng.com/company/>.
- [2] European Commission, GREEN PAPER on the impact of Transport on the Environment - A Community strategy for "sustainable mobility".
- [3] International Energy Agency, "Key World Energy Statistics 2020".
- [4] International Energy Agency, "Emissions from transport continue to rise", <https://www.iea.org/topics/transport>.
- [5] International Energy Agency, "Electric vehicles have been growing around the world", <https://www.iea.org/topics/transport>.
- [6] Bockris Vol. 2, p. 855.
- [7] <https://www.psmarketresearch.com/market-analysis/cathode-material-automotive-lithium-ion-battery-market>.
- [8] OCVfunction Hanane Hemi, N. M'Sirdi, Aziz Naamane. Open Circuit Voltage of a Lithium ion Battery Model adjusted by data fitting. IRSEC 2018, Dec 2018, Rabat, Morocco. hal-01956283.
- [9] Q. Wang, P. Ping, X. Zhao, G. Chu, J. Sun, C. Chen, Thermal runaway caused fire and explosion of lithium ion battery, *Journal of Power Sources* 208 (0) (2012) 210-224.
- [10] Vidal, Carlos ; Gross, Oliver ; Gu, Ran ; Kollmeyer, Phillip ; Emadi, Ali, xEV Li-Ion Battery Low-Temperature Effects-Review, *IEEE transactions on vehicular technology*, 2019-05, Vol.68 (5), p.4560-4572.
- [11] <https://www.arbin.com/products/battery-test-equipment/>.
- [12] Anthony Barré, Benjamin Deguilhem, Sebastien Grolleau, Mathias Gérard, Frédéric Suard, et al.. A review on lithium-ion battery ageing mechanisms and estimations for automotive applications. *Journal of Power Sources*, Elsevier, 2013, 241, pp.680 - 689. 10.1016/j.jpowsour.2013.05.040. cea-01791260
- [13] P. Balakrishnan, R. Ramesh, T. P. Kumar, Safety mechanisms in lithium-ion batteries, *Journal of Power Sources* 155 (2) (2006) 401 · 414.
- [14] D. Goers, M. E. Spahr, A. Leone, W. Märkle, P. Novák, The influence of the local current density on the electrochemical exfoliation of graphite in lithium-ion battery negative electrodes, *Electrochimica Acta* 56 (11) (2011) 3799 · 3808.

- [15] S. Zhang, M. S. Ding, K. Xu, J. Allen, T. R. Jow, Understanding solid electrolyte interface film formation on graphite electrodes, *Electrochemical and Solid State Letters* 4 (2001) 206-208.
- [16] Christoph R. Birkl, Matthew R. Roberts, Euan Mcturk, Peter G. Bruce, and David A. Howey. "Degradation diagnostics for lithium ion cells" *Journal of Power Sources*, vol. 341, 2016. doi:10.1016/j.jpowsour.2016.12.011
- [17] S. Bashash, S. J. Moura, J. C. Forman, H. K. Fathy, Plug-in hybrid electric vehicle charge pattern optimization for energy cost and battery longevity, *Journal of Power Sources* 196 (1) (2011) 541 · 549.
- [18] <https://www.upsbatterycenter.com/blog/lithium-plating/>
- [19] B. L. Ellis, K. T. Lee, L. F. Nazar, Positive electrode materials for li-ion and li-batteries, *Chemistry of materials* 22 (2009) 691-714.
- [20] N. Andrenacci, V. Sglavo, F. Vellucci, Definizione della procedura sperimentale di invecchiamento delle celle litio-ione, Report RdS/PAR2015/194.
- [21] Matthieu Dubarrya, Cyril Truchota, Bor Yann Liaw, Kevin Gering, Sergiy Sazhin, David Jamison, Christopher Michelbacher, Evaluation of commercial lithium-ion cells based on composite positive electrode for plug-in hybrid electric vehicle applications. Part II. Degradation mechanism under 2 C cycle aging, *Journal of Power Sources* Volume 196, Issue 23, 1 December 2011, Pages 10336-10343.
- [22] AutoLion - Electrochemical Lithium-ion Battery Model.
- [23] Hosseinzadeh, E. Marco, J. Jennings, P. Electrochemical-Thermal Modelling and Optimisation of Lithium-Ion Battery Design Parameters Using Analysis of Variance. *Energies* 2017, 10,1278,doi:10.3390/en10091278.
- [24] Majid Astaneh, Jelena Andric, Lennart Löfdahl, Dario Maggiolo, Peter Stopp, Mazyar Moghaddam, Michel Chapuis and Henrik Ström, Calibration Optimization Methodology for Lithium-Ion Battery Pack Model for Electric Vehicles in Mining Applications.
- [25] Santhanagopalan, S.; Guo, Q.; White, R.E. Parameter Estimation and Model Discrimination for a Lithium-Ion Cell. *J. Electrochem. Soc.* 2007, 154, A198, doi:10.1149/1.2422896.